


Article

Mechanistic Morphogenesis of Organo-Sedimentary Structures Growing Under Geochemically Stressed Conditions: Keystone to Proving the Biogenicity of Some Archaean Stromatolites?

Keyron Hickman-Lewis ^{1,2,*} , Pascale Gautret ^{3,*}, Laurent Arbaret ³, Stéphanie Sorieul ⁴, Rutger De Wit ⁵, Frédéric Foucher ¹, Barbara Cavalazzi ^{2,6} and Frances Westall ¹

¹ CNRS Centre de Biophysique Moléculaire, 45071 Orléans, France

² Dipartimento di Scienze Biologiche, Geologiche e Ambientali, Università di Bologna, I-40126 Bologna, Italy

³ Université d'Orléans, CNRS, BRGM, ISTO, Institut des Sciences de la Terre, 45071 Orléans, France

⁴ Université de Bordeaux, CNRS, IN2P3, CENBG, 33175 Gradignan, France

⁵ MARBEC, Université de Montpellier, CNRS, IRD, Ifremer, 34095 Montpellier, France

⁶ Department of Geology, University of Johannesburg, Auckland Park 2006, Johannesburg, South Africa

* Correspondence: keyron.hickman-lewis@cnrs-orleans.fr (K.H.-L.); pascale.gautret@cnrs-orleans.fr (P.G.)

Received: 18 June 2019; Accepted: 14 August 2019; Published: 16 August 2019



Abstract: Morphologically diverse organo-sedimentary structures (including microbial mats and stromatolites) provide a palaeobiological record through more than three billion years of Earth history. Since understanding much of the Archaean fossil record is contingent upon proving the biogenicity of such structures, mechanistic interpretations of well-preserved fossil microbialites can reinforce our understanding of their biogeochemistry and distinguish unambiguous biological characteristics in these structures, which represent some of the earliest records of life. Mechanistic morphogenetic understanding relies upon the analysis of geomicrobiological experiments. Herein, we report morphological-biogeochemical comparisons between micromorphologies observed in growth experiments using photosynthetic mats built by the cyanobacterium *Coleofasciculus chthonoplastes* (formerly *Microcoleus*) and green anoxygenic phototrophic *Chloroflexus* spp. (i.e., *Coleofasciculus–Chloroflexus* mats), and Precambrian organo-sedimentary structures, demonstrating parallels between them. In elevated ambient concentrations of Cu (toxic to *Coleofasciculus*), *Coleofasciculus–Chloroflexus* mats respond by forming centimetre-scale pinnacle-like structures (supra-lamina complexities) associated with large quantities of EPS at their surfaces. μ PIXE mapping shows that Cu and other metals become concentrated within surficial sheath-EPS-*Chloroflexus*-rich layers, producing density-differential micromorphologies with distinct fabric orientations that are detectable using X-ray computed micro-tomography (X-ray μ CT). Similar micromorphologies are also detectable in stromatolites from the 3.481 Ga Dresser Formation (Pilbara, Western Australia). The cause and response link between the presence of toxic elements (geochemical stress) and the development of multi-layered topographical complexities in organo-sedimentary structures may thus be considered an indicator of biogenicity, being an indisputably biological and predictable morphogenetic response reflecting, in this case, the differential responses of *Coleofasciculus* and *Chloroflexus* to Cu. Growth models for microbialite morphogenesis rely upon linking morphology to intrinsic (biological) and extrinsic (environmental) influences. Since the pinnacles of *Coleofasciculus–Chloroflexus* mats have an unambiguously biological origin linked to extrinsic geochemistry, we suggest that similar micromorphologies observed in ancient organo-sedimentary structures are indicative of biogenesis. An identical *Coleofasciculus–Chloroflexus* community subjected to salinity stress also produced supra-lamina complexities (tufts) but did not produce identifiable micromorphologies in three dimensions since salinity seems not to negatively impact either organism, and therefore cannot be used as a morphogenetic tool for the interpretation of density-homogeneous micro-tufted

mats—for example, those of the 3.472 Ga Middle Marker horizon. Thus, although correlative microscopy is the keystone to confirming the biogenicity of certain Precambrian stromatolites, it remains crucial to separately interrogate each putative trace of ancient life, ideally using three-dimensional analyses, to determine, where possible, palaeoenvironmental influences on morphologies. Widespread volcanism and hydrothermal effusion into the early oceans likely concentrated toxic elements in early biomes. Morphological diversity in fossil microbialites could, therefore, reflect either (or both of) differential exposure to ambient fluids enriched in toxic elements and/or changing ecosystem structure and tolerance to elements through evolutionary time—for example, after incorporation into enzymes. Proof of biogenicity by deducing morphogenesis (i.e., a process preserved in the fossil record) overcomes many of the shortcomings inherent to the proof of biogenicity by descriptions of morphology alone.

Keywords: microbial mat; stromatolite; anoxygenic photosynthesis; X-ray micro-scale computed tomography; Archaean; early life; Dresser Formation; Middle Marker horizon

1. Introduction

Organo-sedimentary structures (OSS) of microbial origin include microbial mats (complex, laminated, sediment-binding ecosystems), biofilms (the individual, surface-attached, laminar components of microbial mats), stromatolites (biosedimentary structures accreting from a locus and driven by concomitant mat growth and mineral precipitation), and microbially induced sedimentary structures (MISS; sedimentary textures recording the prior presence of microbial mats or biofilms). Together, these present an archive of biology and palaeobiological processes through more than three quarters of Earth's history (e.g., [1–7]). Such structures are usually constructed by phototrophic microorganisms that require ready access to sunlight and, therefore, form in shallow water environments. In the geological record, OSS are usually preserved as biolaminites, organic-rich laminations within sediments [8,9], or as stromatolites, laminated, usually carbonate- or silica-preserved structures charting the co-occurrence of biomass growth and mineral precipitation [2,4,10]. Most importantly, OSS reflect biological communities presumed to have played a significant role in biogeochemical cycling through time, particularly during early Earth history [4,11–13]. This may be by virtue of their occurrence in shallow-water environments at the interface of the hydrosphere, geosphere, and atmosphere. Although phototrophic microbes may have been the primary producers and mat-forming organisms, OSS comprise an assemblage of microcolonies varying in both lateral and vertical distribution [14,15], and may contribute measurably to multiple biogeochemical cycles. In modern and ancient settings alike, OSS encompass wide morphological variation [3,7,9,16–18], the reasons for which remain incompletely appraised. Herein, we suggest that the origins of diverse OSS morphologies may be explained by defining the morphogenetic factors driving their shapes, i.e., the growth processes preserved in their morphologies. This approach may overcome the ambiguity in assessing the origins of OSS using only morphology, which has historically led to uncertainty in the distinction of processes related to biology from those exclusively reflecting environmental factors.

Morphogenesis of Organo-Sedimentary Structures

Pulsed and cyclical *in vivo* changes of form are typical growth phenomena in biotic systems at both the organismal and community scale. The diversity of morphology in microbial OSS should be explicable through identifying the drivers of change, and a number of holistic mathematical models linking microbial mat and stromatolite morphogenesis to biophysical, physiological, and palaeoenvironmental parameters have sought to describe these processes [19–32]. Such studies have highlighted that the necessary framework for understanding the morphogenesis of OSS should incorporate basic features of microbial growth (intrinsic factors) and its responses to environmental variables (extrinsic

factors) [4,10,22,24,26,31,33]. Intrinsic factors include growth rates, structural accretion by sediment trapping and binding (biostabilisation), mineral precipitation, community or trophic structure through time, quorum sensing and organismal collaboration and competition, elemental cycling and exopolymer composition, and adhesiveness. Extrinsic factors include nutrient availability, seawater chemistry, hydrodynamic stresses and shear, together with sedimentation rates and burial.

What factors determine the eventual morphospace of OSS and what are the interrelationships between physicochemical drivers? To what extent do hydrodynamic, biophysical, or geochemical forcings govern OSS? Can mechanistic morphogenetics distinguish between biotic and abiotic origins for controversial OSS from the Archaean fossil record? Endeavours to model or experimentally grow OSS have, as their objective, the identification of a set of factors that uniquely reflect biological activity [24,28,29,33]. These factors are non-linear and non-determinative, and form a network of interdependent forcings, the resulting structures being microbially derived laminations of alternating composition. Geomicrobiological appraisals of modern microbial mats [33,34], growth experiments [27,28,32], and image analysis [23–25] provide both the ‘raw material’ for quantitative morphogenetic and morphometric analyses and a qualitative framework within which fossil OSS may be interpreted. Biogeochemical processes observed in natural and experimental environments have been incorporated into mathematical growth models, aiding in the definition of parameters relevant to any framework for microbialite morphogenesis. It is conceivable that recognisable, unambiguously biological, and predictable morphogenetic indicators may emerge from the fossil record. We use the terminology determined by these observation-based models to discuss our comparative morphogenesis approach (defined in the following text).

Growth models of OSS fall broadly into three categories. The first involves variants on the Kardar–Parisi–Zhang (KPZ) equation [35], a three-dimensional (3D) Eden growth model, which may be qualitatively stated as the definition of each term:

Change of height with time = upward growth velocity + interfacial growth in the normal direction + erosional and sedimentational smoothing + uncorrelated random noise.

The noise term reflects stochastic environmental fluctuations. Batchelor et al. [23,24] criticised this equation as failing to adequately consider bulk biological behaviour (e.g., phototaxis) and modified the equation into the deterministic KPZ, which may be qualitatively stated as:

Change of height with time = surface relaxation + interfacial growth in the normal direction + upward growth velocity.

The deterministic KPZ proposed by Batchelor et al. [23] includes no randomness [24], and is thus dependent upon the parameters of the primary baseline. It has been suggested to be unsuitable for recreating biogenic overhanging forms [26,36], but certain interlinked intrinsic and extrinsic factors can nonetheless be extracted. Batchelor et al. [25] found that models with upward growth < interfacial growth produced broader, domical structures, whereas models with interfacial growth < upward growth produced angular conical structures. The thickening of laminations at the crest region evidences phototactic behaviour, thus validating photosynthesis as a major primary metabolic pathway in many OSS.

The second basis for models is diffusion-controlled growth (diffusion-limited aggregation (DLA) and diffusion-reaction). DLA involves Brownian particle motion able to form aggregative, fractal-like clusters reflecting microstromatolites depending upon the availability of environmental particles. Diffusion control of growth reflects the principal ‘extrinsic’ effect on stromatolite morphogenesis: material or molecular flux encouraging growth (e.g., [29,30,33]). The growth vector is a function of diffusion rate through the mat volume, which is determined by mat thickness, curvature, the ratio of mat thickness to curvature, and surface normal growth [30]. The rate of mineral precipitation scales with diffusive flux, and since regions of greater curvature allow chemical flux through a larger

surface area, they will grow more rapidly [30]. This diffusion–reaction model thus reproduces conical stromatolite morphologies with lamination specificities, i.e., thickened crest regions.

The third modelling approach applies various life rules related to the evolution of cellular automata (CA), broadly defined as cell system characteristics and interactions on the local scale (microscale) that govern the global (macroscale) biological system. Dupraz et al. [26] combined the DLA model (extrinsic effects) with simple aspects of CA (intrinsic effects), yielding a DLA-CA model to explain branching Proterozoic forms. By varying substrate morphology and including community cell-relation phenomena, such as inter-cell dynamics, links between biology and the environment may be quantified (see [33]).

The reader will, at this point, recognise that, while differing in their approaches, models of OSS growth answer common questions and are resoundingly useful in defining the natural processes that dominate OSS development. We consider that biological influence is generally neglected relative to environmental influence and, where biogenicity is controversial, as in some Archaean OSS, this may result in overly cautious interpretation even when structures are virtually indistinguishable from younger biological forms [4,10]. Further complexity is added by the fact that, over the course of several months, microbial mats develop distinctive three-dimensional micromorphologies provided no sedimentary influx suffocates the system [9]. Such a complex climax consortium evidences the temporal evolution of a biotic system and is not exclusively upward as modelled, but incorporates biological complexities including competition and collaboration. For example, microbial mats are tiered by autotrophic and heterotrophic metabolisms during the formative and consuming stages [8], producing lamina-scale phenotypes. At the lamination scale, much information may be extracted from the fossil record of OSS to explain the interaction of microbial mats with their environments in deep time. Consequently, strong criteria for the biogenicity of ancient OSS may be found at the scale of individual laminae.

In this study, we aim to evaluate the biological origin of Archaean OSS based on 3D correlative microscopy of comparable microstructures formed by modern microbial communities containing dense populations of filamentous organisms that may reflect non-oxygenic phototrophic (non-cyanobacterial) communities from the Palaeoarchaeon [11]. We describe microstructures associated with modern living microbial communities growing under environmental stresses: environments enriched in toxic elements and with elevated salinity. This permits us to demonstrate that correlative geomicrobiological, morphological, and geochemical analysis of samples in three dimensions has the potential to establish the biogenicity of Precambrian structures within a morphogenetic framework inspired by the interrelation of processes defined by observation and modelling. Such an approach contributes to a unified morphogenetic theory for OSS incorporating intrinsic ecophysiology and extrinsic palaeoenvironmental factors.

2. Materials and Methods

2.1. Geomicrobiology and Geochemistry (Modern Samples)

Photosynthetic microbial mats built by the cyanobacterium *Coleofasciculus chthonoplastes* (formerly known as *Microcoleus chthonoplastes*, see [37]; hereafter referred to as *Coleofasciculus*) and the green anoxygenic phototrophs *Chloroflexus* spp. (i.e., *Coleofasciculus*–*Chloroflexus* mats) were collected in April 2011 (sample 805; Figure 1C–E) and February 2012 (sample 1011; Figure 1F–G) from the hypersaline lake La Salada de Chiprana, NE Spain (N 41°14′21.8″ W 0°11′10.9″) at water depths of 25–50 cm (Figure 1A,B). Sample 805 was flat-laminated, whereas sample 1011 showed natural pinnacle formation due to high salinity (120 g/L^{−1}) resulting from the particularly dry year 2011. Sample 805, which showed a smooth surface without pinnacles, was collected during favourable ambient conditions and transported alive to the laboratory for culturing experiments. Sample 1011 was directly fixed in glutaraldehyde and conserved as a representation of a highly stressed community.

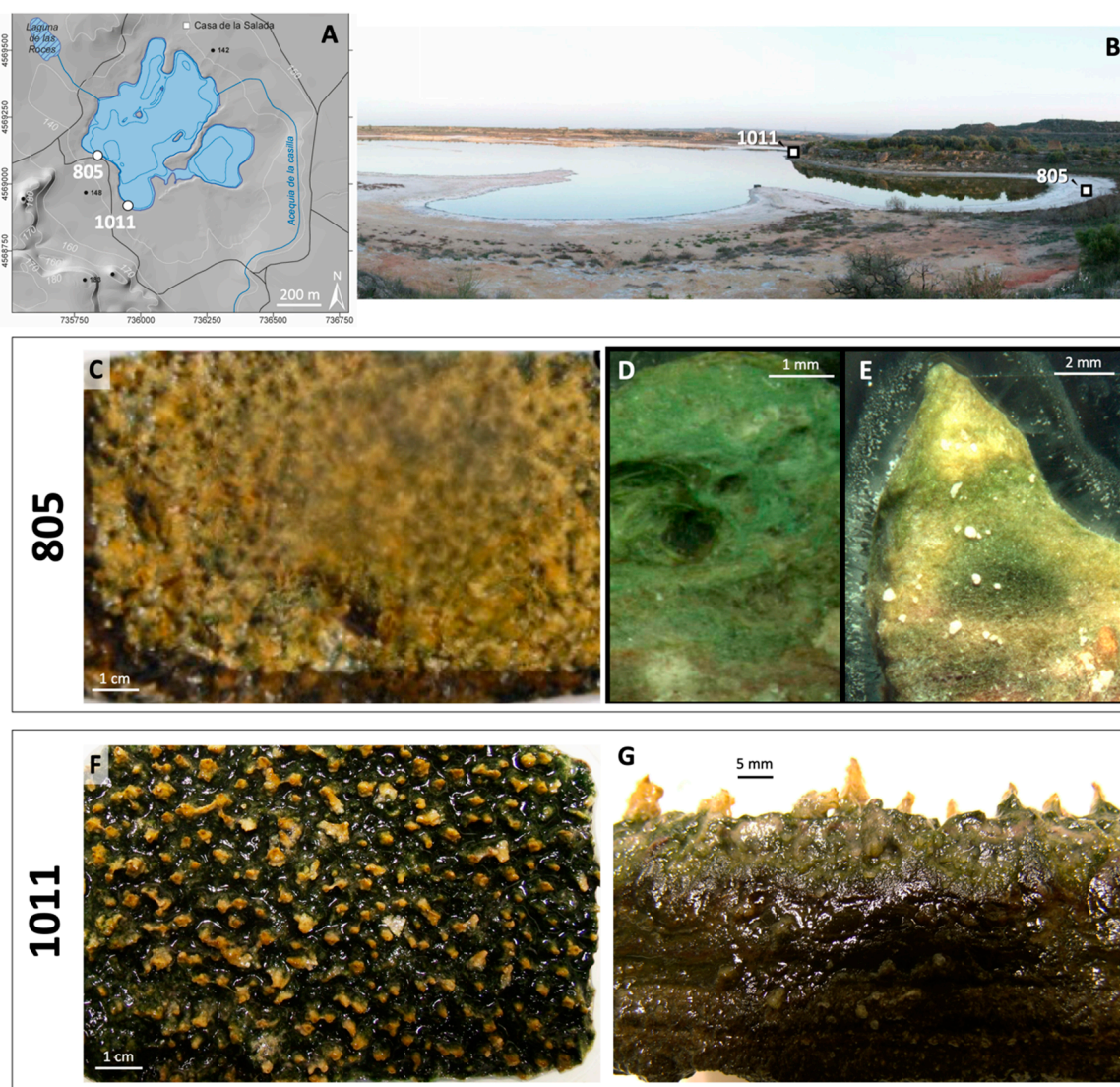


Figure 1. Modern microbialite samples and collection locality. (A) Map showing extent of La Salada Chiprana during the collection periods. Sample locations indicated. (B) Field photograph of La Salada Chiprana. (C) Original field sample of microbial mat 805 before culturing. (D) Section through field sample 805 before culturing. (E) Representative large pinnacle-like structure (supra-lamina complexity) that developed in the Cu-enriched medium (sample 805-Cu); similar structures were studied by SEM (Figure 2G–L, 3), PIXE (Figure 4) and X-ray μ CT (Figure 5). (F,G) Sample 1011. (F) Original field sample of microbial mat 1011, exhibiting natural tuft-like convexities as a result of elevated salinity in La Salada Chiprana. (G) Cross-section view through sample 1011, showing stratification of the microbial community and millimetre-scale tufts. A fragment of this sample was studied by X-ray μ CT (Figure 6).

Subsamples of field sample 805 were cultured for six months in aquaria enriched in Fe and Mn at different concentrations at ambient temperatures. The aquaria were subjected to a diel cycle of 12-hour light under a Philips-HPI T Plus 400 W lamp and 12-hour darkness. Photosynthetically active radiation (PAR) intensity (light intensity when photosynthesis occurs, measured as the amount of energy in light wavelengths between 400 and 700 nm) was $167 \mu\text{mol}\cdot\text{m}^{-2}\cdot\text{sec}^{-1}$ (LiCor 250A photometer equipped with a LI-190SA Quantum Sensor). Synthetic seawater solutions (Ocean Instant) were enriched with $10 \text{ mg}\cdot\text{L}^{-1}$ Fe, $10 \mu\text{g}\cdot\text{L}^{-1}$ Cu and $10 \mu\text{g}\cdot\text{L}^{-1}$ Mn (sample 805-Fe), and $5 \text{ mg}\cdot\text{L}^{-1}$ Cu, $10 \mu\text{g}\cdot\text{L}^{-1}$ Fe and $10 \mu\text{g}\cdot\text{L}^{-1}$ Mn (sample 805-Cu), using commercially available chemicals ($\text{CuSO}_4\cdot 5\text{H}_2\text{O}$, $\text{N}_2\text{O}_9\text{Fe}_9\text{H}_2\text{O}$, and $[\text{CH}_3\text{COO}]_2\text{Mn}\cdot 4\text{H}_2\text{O}$). In all cases, these solutions produced a medium with mildly alkaline pH (7.2–8.0).

The biomass and photosynthetic activity of both the *Coleofasciculus* and *Chloroflexus* microbial communities were measured using FRe (Fluorescence Induction and Relaxation) fluorometry (Satlantic Inc.) [38] fitted with a Satlantic fibre optic probe attachment. The oxygenic photosynthetic response of cyanobacteria (*Coleofasciculus*) was traced at 680 nm (Photosystem II fluorescence [38]), while the photochemistry of anoxygenic photosynthetic bacteria (purple sulfur and green non-sulfur bacteria, Chloroflexaceae) was characterised by monitoring the fluorescence signal at 880 nm (fluorescence of the Bacteriochlorophyll-*a*-containing type II reaction centres in Chloroflexaceae) [39]. Measurements ($n = 7$ for each treatment) were performed after 4 weeks' incubation and at the end of the experiment (after 24 weeks' incubation) with the emitting blue diode placed 0.7 ± 0.1 cm above microbial mat surface.

Liquid-N₂ cryofixed and lyophilised samples of all studied mats (samples 805, 805-Fe, 805-Cu, and 1011) were observed using a Hitachi TM3000 SEM (ISTO-Orléans) (Figures 2 and 3). The same cut sections of some of these microbial mats (samples 805-Fe and 805-Cu) were mounted on carbon adhesive discs for *in situ* particle-induced X-ray emission (PIXE) elemental analysis using the microbeam line of the AIFIRA facility at CNRS-CENBG (CNRS Bordeaux-Gradignan). For comparative purposes, we detail the findings from the mats grown in solutions enriched in Fe and Cu (Figure 4). μ PIXE analyses were performed using a 3 MeV proton beam for 60–90 min. The experimental setup comprised two PIXE detectors and one RBS detector; both PIXE detectors were equipped with a 500 μ m 'Funny Filter' with a 2 mm diameter hole size. Samples 805-Cu and 1011 were then mounted for X-ray micro-scale computed tomography (μ CT) analysis to observe their 3D interior structures (Figures 5 and 6).

2.2. Microbial Palaeontology (Precambrian Samples)

A second, comparative sample set, consisting of two Precambrian OSS sourced from the East Pilbara terrane of Western Australia (domical–conical stromatolites from the 3.481 Ga Dresser Formation, sample 00AU23, hereafter DF1) and the Barberton greenstone belt of South Africa (micro-tufted microbial mats from the 3.472 Ga Middle Marker horizon, sample 07SA23, hereafter MM1), both of which exhibit, at different scales, complex surface topographies (Figures 7 and 8), was used as a comparative dataset. The OSS of both the Dresser Formation and Middle Marker horizon have been deemed biological in origin [7,40].

Correlated three-dimensional reconstructions and geochemical studies of the modern samples were used as a framework within which to interpret these Precambrian OSS. Since SEM imaging and EDS elemental analyses of these Precambrian samples yield little complementary information to aid comparison with the modern dataset due to chemical dilution resulting from extreme and early silicification, we report the morphology and mineralogy of Precambrian OSS using optical microscopy and Raman spectroscopy. Optical microscopy used an Olympus BX-51 (CNRS-Orléans).

2.3. Raman Spectroscopy (Precambrian Samples)

Raman spectroscopy was conducted with a WITec Alpha500 RA system using a frequency-doubled Nd: YAG green laser (wavelength 532 nm) at CNRS-CBM (CNRS Orléans). The system used a motorised table to move the sample continuously below a laser beam focussed onto the sample *via* a microscope objective. Spectra form a dataset, spatially referenced over the scanned area, was processed to obtain compositional maps. Compounds were then represented either by different colours or as concentration maps according to intensity. A detailed explanation of Raman mapping can be found in Foucher et al. [41]. Scanning parameters are reported in the caption of Figure 9.

2.4. Micro-Scale X-ray Computed Tomography (Modern and Precambrian Samples)

Flexible possibilities in sample preparation mean that X-ray μ CT was applied to both modern (Figures 5 and 6) and Precambrian samples (Figures 10–12), and therefore forms the direct link for morphometric comparisons between the two. Sample 805-Cu was prepared as a lyophilised fragment of a ~7 mm pinnacle from the upper surface of a microbial mat (Figure 5A). Sample 1011 was prepared as a cut fragment of glutaraldehyde-fixed mat including a ~6 mm tuft (Figure 6A,B). A cylinder

of 8 mm diameter was cut through a macroscopically visible domical structure from the Dresser Formation (sample DF1) and a cylinder of 2 mm was cored through a microbial mat sequence from the Middle Marker horizon (sample MM1). X-ray CT scanning was conducted at CNRS-ISTO (CNRS Orléans) using a 180 NF Phoenix Nanotom, operating with an accelerating voltage of 180 kV, a filament current of 170 nA, and an operating voltage of 120 V (see figure captions for acquisition parameters). Attenuation of the X-ray beam passing through the sample is dependent on sample characteristics [42–44]. The choice of scanning parameters reflects the variations in size and X-ray density of the sample. The voltage and current of the X-ray source were controlled in order to keep the former as low as possible to achieve maximum composition-based contrast, whilst allowing sufficient penetration to scan the entirety of the sample volume. The interested reader can find a comprehensive overview of tomographic analysis in Sutton et al. [44]. The distance of the sample from the X-ray source controls the number of X-rays passing through the sample and, thus, the resolution, i.e., a sample mounted closer to the X-ray source will scan at a higher resolution. During the acquisition, the turntable rotates, and each view is taken at an interval of 360° divided by the total number of projections with an image size of 2304×2304 pixels. For our samples, the total number of projections ranged between 1200 and 2000 and the resolution from 1.19 to $6.89 \mu\text{m}$ per pixel. Sectional images of the samples were reconstructed by determining the attenuation coefficients for each line of pixels using Beer's law, generating a stack of slices corresponding to successive 2D sections of the sample. Corrections were applied in order to reduce the effects of beam hardening, ring artefacts, and misalignment. The 3D volumes of each phase were extracted from the stack of sectional images using the segmentation tool of VG-Studio Max software (Volume Graphics).

3. Results

3.1. Modern Samples

3.1.1. Macrophotography, Optical Light Microscopy, SEM, and FIRE Photochemistry

Coleofasciculus and *Chloroflexus* were present throughout the microbial stratigraphy of field sample 805 (before culturing), although *Coleofasciculus* dominated the surface layer while *Chloroflexus* was more common at depth (Figure 2M–O). Light microscopy and SEM observations of the micromorphological characteristics of cultured subsamples of 805 after a 24-week incubation period are shown in Figure 2, for both the experiments in Fe-enriched (sample 805-Fe; Figure 2A–F) and Cu-enriched saline water (sample 805-Cu; Figure 2G–L). Under Fe enrichment (sample 805-Fe), the macroscopic morphology and community structure of the mat did not change with respect to the field sample 805. In contrast, samples incubated in Cu-enriched aquaria (sample 805-Cu) developed large pinnacle-like structures within several days (Figure 1E, 3A–C), i.e., the surface topography changed during Cu incubation, and the morphology and community structure of 805-Cu mats were different to field sample 805 and cultured sample 805-Fe. In the 805-Fe subsample, as in field sample 805, the upper green layer was dominated by oxygen-producing *Coleofasciculus* trichomes (Figure 2C,F) and rare sheaths (Figure 2D), whereas the lower darker layers were rich in the green anoxygenic phototroph *Chloroflexus* (Figure 2F). In contrast, the mat between the pinnacles of 805-Cu showed an inverted community structure, where the cyanobacterial *Coleofasciculus* layer was at depth (Figure 2L), overlain by a surficial layer of densely packed *Coleofasciculus* sheaths with EPS and *Chloroflexus* filaments (Figure 2I–K). The same inverted community structure was observed in pinnacles: the inner *Coleofasciculus*-rich biomass is overlain by a thin layer of *Chloroflexus* and EPS (Figure 3A–C).

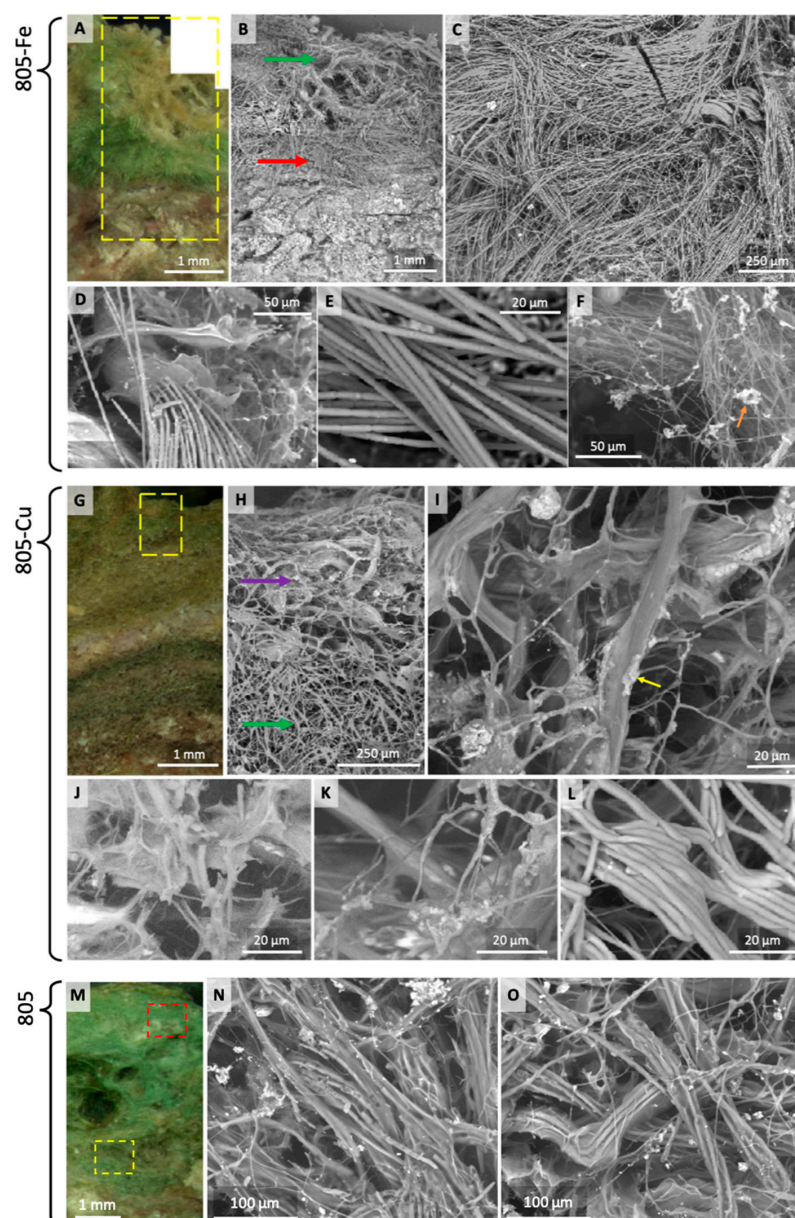


Figure 2. Micromorphological characteristics of microbial mat sample 805 after a 24-week incubation period in (A–F) Fe-enriched saline water (sample 805-Fe) and (G–L) Cu-enriched saline water (sample 805-Cu). The original field sample 805 is included for comparison (M–O). (A,B) Photograph and SEM micrograph of a vertical cut through mat 805-Fe showing stratification of the community. The upper green layers represent the major photosynthetically active, *Coleofasciculus*-rich layer (green arrow), whereas the lower darker layers represent those rich in the green anoxygenic phototroph *Chloroflexus* (red arrow). Yellow box indicates region imaged in B. (C–E) Main green photosynthetically active layer of *Coleofasciculus* trichomes, large portions of which are outside the sheaths, and with very low densities of EPS. (C,E) Restricted portions with trichomes, sheaths, and EPS fibrillar networks. (F) *Chloroflexus*-rich layer at the base of the upper green layer, with iron oxide (orange arrow) precipitation on filaments. (G) Vertical cut through mat 805-Cu, showing community stratification, with the green *Chloroflexaceae* bacteria overlying the cyanobacterial layer dominated by *Coleofasciculus*. Yellow box indicates region imaged in H. (H) SEM micrograph showing the interface between the surficial sheath-rich layer (purple arrow) with EPS and *Chloroflexus* filaments (the sheath-EPS-*Chloroflexus* layer) and the underlying green, *Coleofasciculus*-rich layer (green arrow). (I–K) Characteristics of the surface layer, composed mostly of sheaths accumulating Cu

deposits (example arrowed) and web-like *Chloroflexus* filaments. (L) *Coleofasciculus*-rich layer beneath the surface layer. Note that the community structure in the Cu-enriched growth experiment is broadly the inverse of that in the Fe-rich growth experiment, with the primary producer (*Coleofasciculus*) being the surficial organism in Fe-rich conditions, but occurring beneath an upper mixed layer of bacteria and bacterial products in Cu-rich growth media. (M–O) Original field sample 805 before culturing in metal-rich aquaria. (M) Photograph of a vertical cut through sample 805, showing the uppermost 5 mm. (N,O) Representative photographs of the sample from the zones indicated by red (N) and yellow (O) boxes. Filaments of *Coleofasciculus* and *Chloroflexus* are well-mixed throughout the uppermost millimetres but note that *Chloroflexus* is considerably more abundant in the lower region (O).

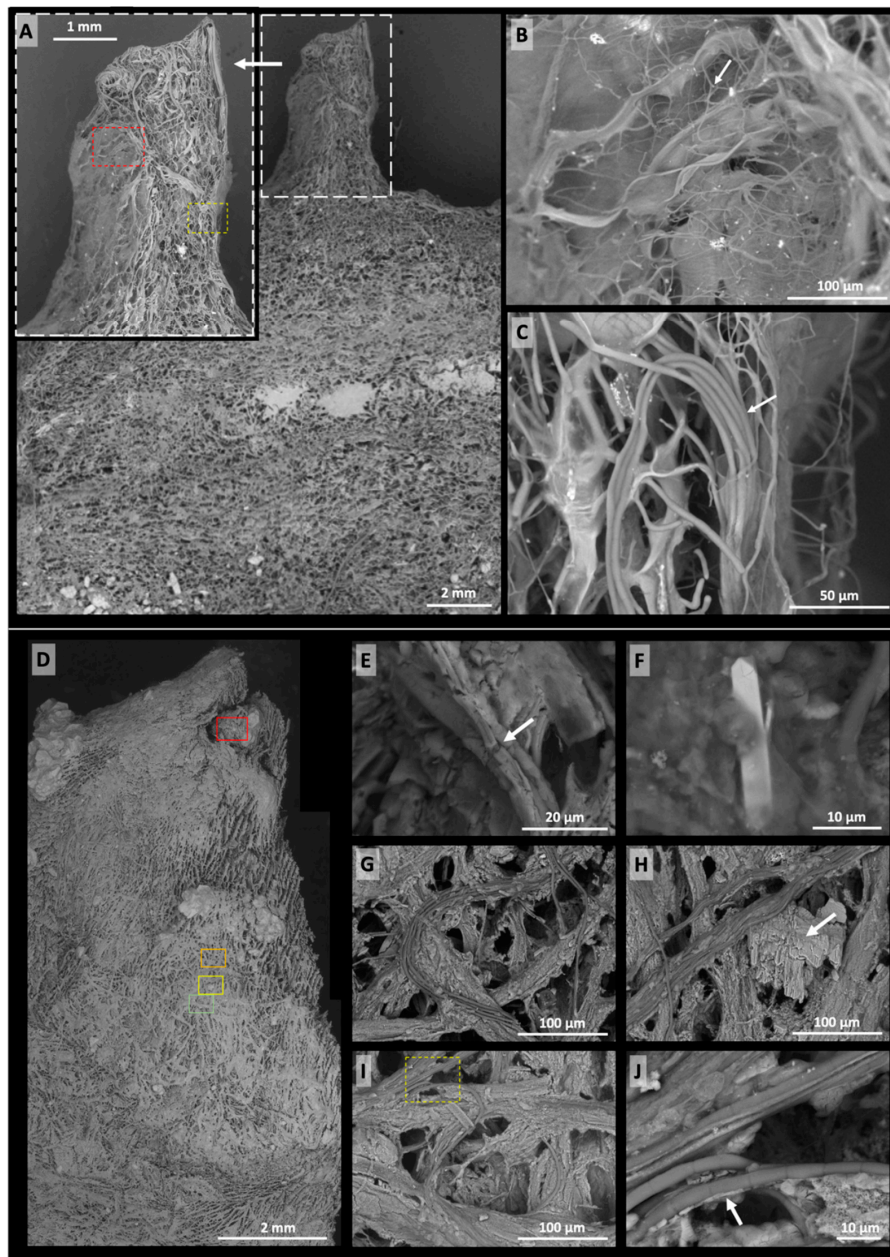


Figure 3. Micromorphological characteristics of supra-lamina complexities in sample 805-Cu (A–C) and sample 1011 (D–J). (A) SEM micrograph of lyophilised microbial mats from sample 805-Cu showing a

cross-section through a representative pinnacle-like convexity. Inset shows high-magnification view. Red box indicates region of B; yellow box indicates region of C. (B) Fine network of *Chloroflexus* filaments (arrowed) at the surface of the pinnacle. (C) Thicker clumps of *Coleofasciculus* filaments (arrowed) in the interior of the pinnacle. (D) SEM micrograph showing a cross-section through a tuft from sample 1011. (E) Broken, distended *Coleofasciculus* filaments (arrow) atop a gypsum grain (from region of red box). (F) Prismatic celestine crystal associated with microbial filaments. (G,H) Well-mixed network of *Coleofasciculus* and *Chloroflexus* filaments with gypsum crystals (example arrowed) that characterises the biomass of the tuft (from regions of orange and yellow boxes). (I,J) Cyanobacterial trichomes (from region of green box) showing incipient mineralisation by gypsum (arrow in J). Yellow box in I shows region of J.

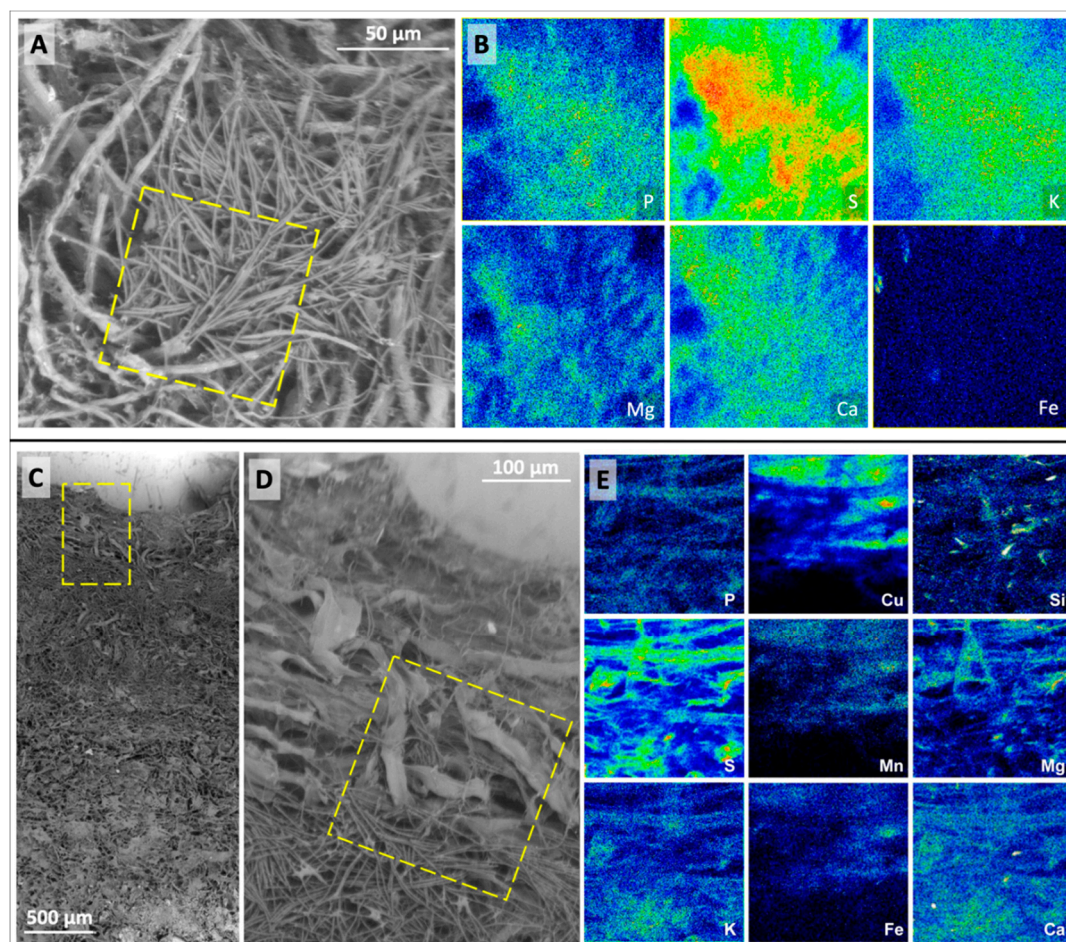


Figure 4. PIXE microbeam elemental mapping of major and trace elements associated with bacterial biomass in samples 805-Fe (A,B) and 805-Cu (C–E). (A) SEM micrograph showing tangled filaments in mats cultured under Fe enrichment (805-Fe). Yellow box indicates region of analysis. (B) Elemental maps of P, S, K, Mg, Ca, and Fe, showing that bio-essential P, S, K, Mg, and Ca are associated with all biomass. Fe, although highly enriched in the culturing medium, is not preferentially concentrated into specific biomass, but distributed throughout the community. (C) SEM micrograph showing stratified microbial mats cultured under Cu enrichment (805-Cu). Yellow box indicates location of D. (D) High-magnification view of the contact zone between the overlying sheath-EPS-*Chloroflexus* layer and the underlying *Coleofasciculus*-dominated layer. Yellow box indicates region of analysis. (E) Elemental maps of P, S, K, Cu, Mn, Fe, Si, Mg, and Ca. Here, the three metallic elements, Cu, Mn, and Fe, are concentrated in the upper sheath-EPS-*Chloroflexus* layer, but are absent from the underlying *Coleofasciculus*-rich layer.

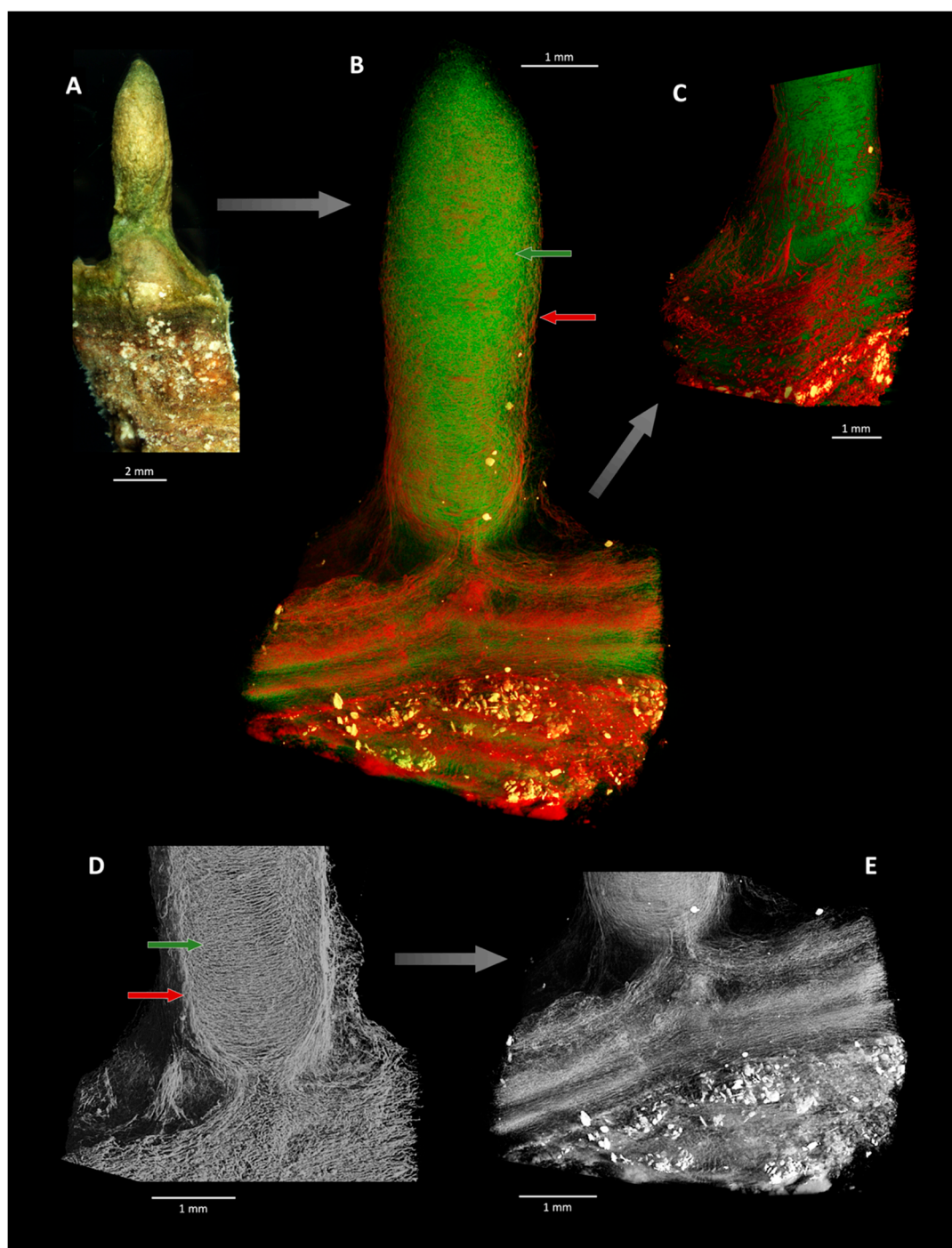


Figure 5. Micro-scale X-ray computed tomography of a lyophilised pinnacle-like structure from sample 805-Cu. **(A)** Photograph of analysed pinnacle. **(B)** Three-dimensional rendering of the same structure, separating three phases: green = filamentous *Coleofasciculus* biomass; red = heavier, metal-enriched biomass corresponding to sheath-EPS-*Chloroflexus*-rich layers; gold = denser mineral phases. Note that the metal-enriched layer rendered in red (red arrow) forms a partial revetment around the less dense pinnacle biomass (green arrow). **(C)** Close up view of pinnacle base. **(D)** Cross-section view through pinnacle showing vertical orientation of filaments in the revetment (red arrow) and horizontal lamination of the inner biomass (green arrow). **(E)** Cross-section view through basal microbial mat material showing filamentous variation and dense particles. Conditions of acquisition: voltage = 120 kV; current = 150 mA; frame acquisition time = 750 ms; number of views = 1200; pixel size = 6.87 μm . Grey arrows indicate correspondence between images.

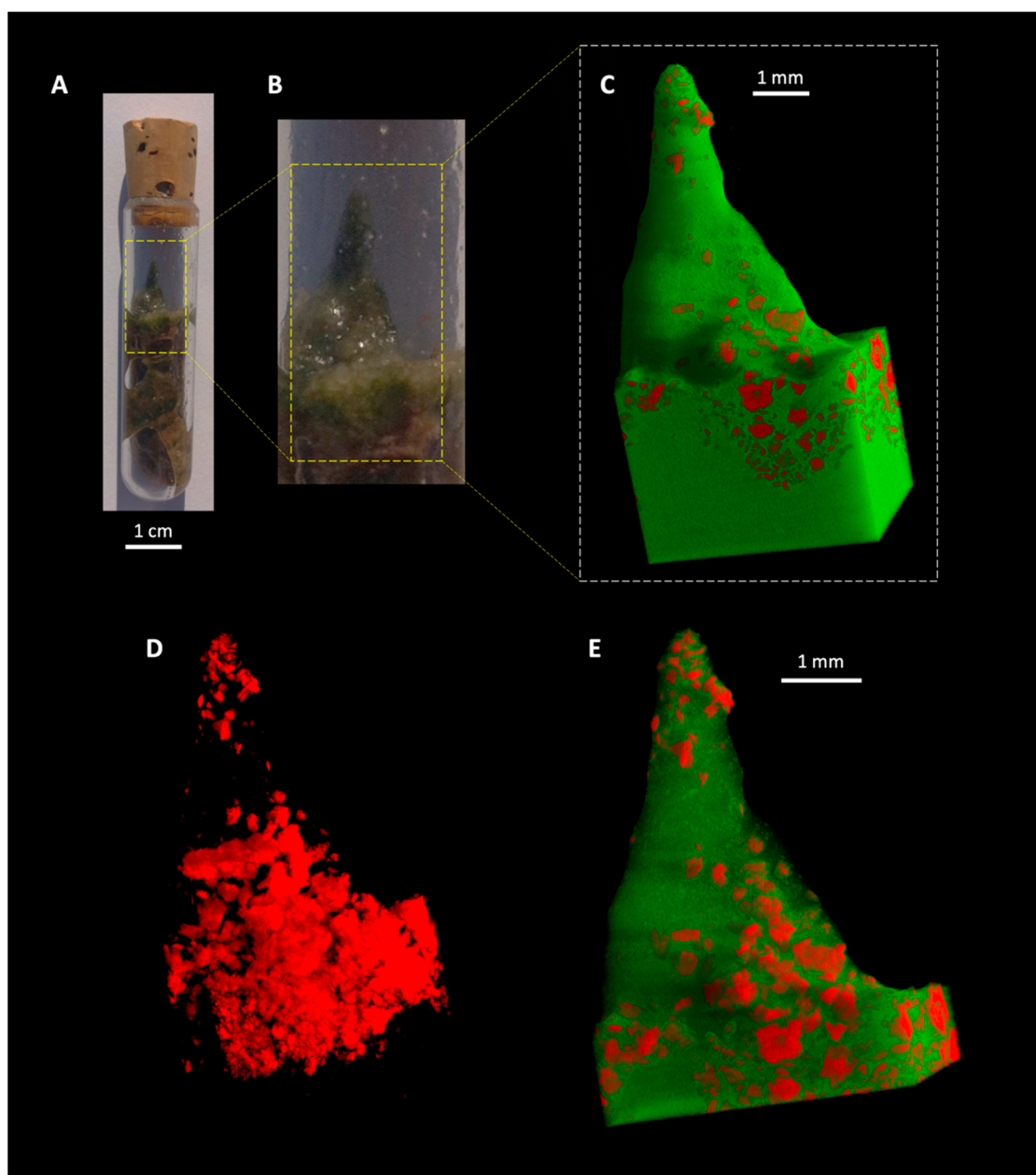


Figure 6. Micro-scale X-ray computed tomography of a glutaraldehyde-fixed tufted microbial mat from sample 1011, grown naturally under high salinity. (A,B) Photographs of sample 1011 contained in a sealed glass tube during analysis to prevent its obliteration due to water content. (C) Three-dimensional rendering of the scanned volume, distinguishing two phases: green = homogeneous biomass; red = gypsum. No fine-scale density contrasts between bacterial biomass exist, i.e., biomass resolves within similar densities (equivalent to green in Figure 7). (D) Distribution of gypsum and celestine within the tuft, i.e., at the base and at the top of the tuft. (E) Relationship of biomass and gypsum and celestine within the tuft, where biomass is rendered semi-transparent. Note that there are no identifiable textural relationships between biomass and salts that indicate fabric formation due to salt stress. Conditions of acquisition: voltage = 120 kV; current = 150 μ A; frame acquisition time = 750 ms; number of views = 1700; pixel size = 6.88 μ m.

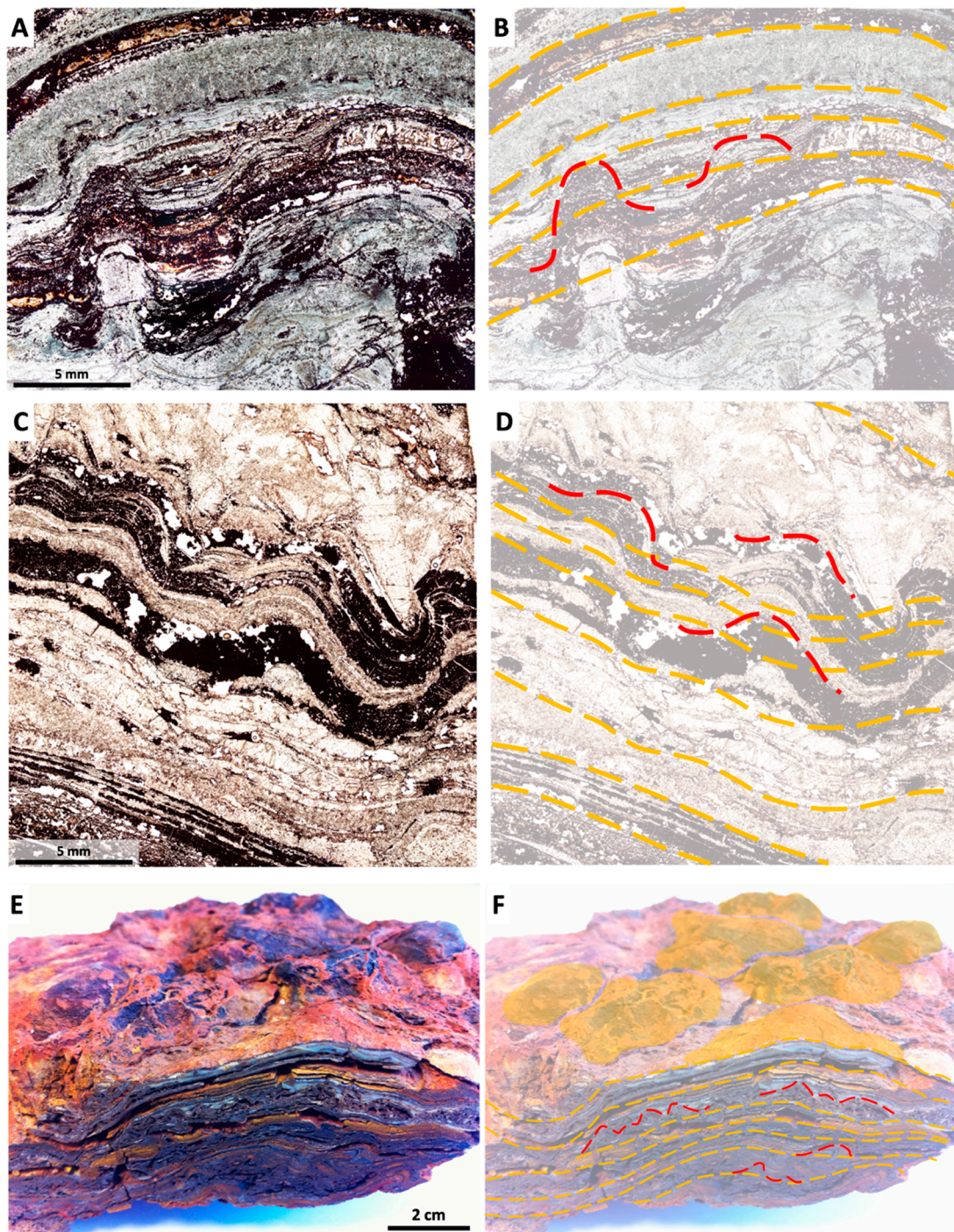


Figure 7. Petrography of 3.481 Ga Dresser Formation organo-sedimentary structures (stromatolites, sample DF1). Images at the left are unaltered, images at the right show interpreted horizons corresponding to a macrostructure with domical macrostructure (gold dashed lines) and the supra-lamina conical complexities arising from certain laminations (red dashed lines). Note the difference in scale of the topography of the macrostructure (centimetre-scale, not wholly observed within the photomicrographs) and supra-lamina complexities (millimetre-scale). (A,B) Photomicrograph of domical stromatolite from which samples were taken for Raman analysis (Figure 9) and X-ray μ CT scanning (Figures 10 and 11). (C,D) Undulating domical stromatolites from a second sample. (E,F) Photograph of representative hand sample with domed upper surface.

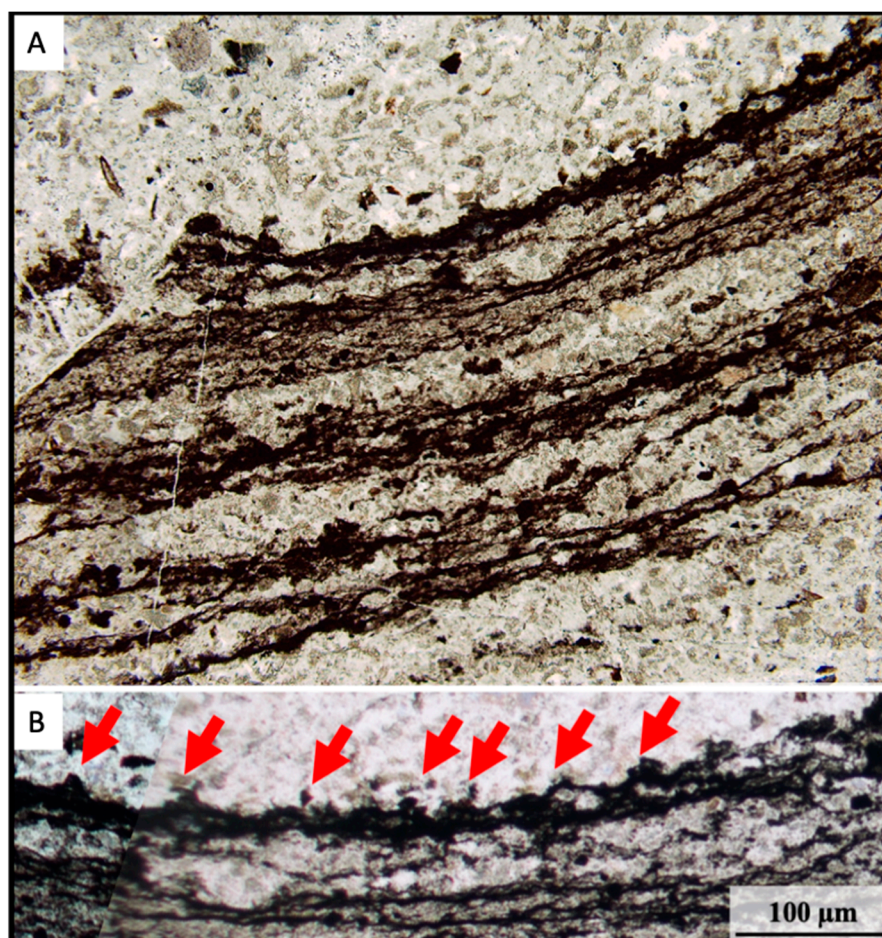


Figure 8. Micro-tufted, multi-laminar microbial mat from the 3.472 Ga Middle Marker horizon (sample MM1), from which samples were taken for Raman analysis (Figure 9) and X-ray μ CT scanning (Figure 12). (A) Wide view (field of view = 2 mm). (B) Close-up view of micro-tufted laminations, each tuft indicated by an arrow.

SEM images of the tufts in sample 1011, which had the same initial biological community as 805, do not show segregation; *Coleofasciculus* and *Chloroflexus* are well-mixed throughout the tuft (Figure 3G–J), although the uppermost biomass is evidently under stress due the presence of gypsum, with individual filaments exhibiting breakage and lysis (Figure 3E). Gypsum and celestine (Figure 3F) are interspersed with biomass throughout the tuft, with a significant concentration of submillimetre scale grains at the top of the pinnacle. Throughout the tuft, filaments show incipient gypsum mineralisation (Figure 3J). The lack of community segregation in sample 1011 (Figure 3D–J) denotes that neither member was adversely affected by salt stress.

Fluorescence Induction Relaxation (FIRE, Ocean Instruments) measurements showed that the biomass and photosynthetic activity of *Coleofasciculus* (traced at 680 nm) did not change in the presence of Fe, but that biomass strongly decreased in the presence of Cu. Both the biomass and photosynthetic response of *Chloroflexus* (traced at 880 nm) increased in the presence of Fe and Cu, particularly in the case of Cu. Hence, we conclude that *Coleofasciculus* is intolerant to Cu, whereas *Chloroflexus* shows tolerance to elevated Cu concentrations. This is consistent with SEM images (Figure 2G–L), which demonstrate that the surficial layer of biomass in the presence of elevated Cu consisted of a dense mixture of sheaths, EPS, and *Chloroflexus* filaments, i.e., reduced *Coleofasciculus* biomass and productivity.

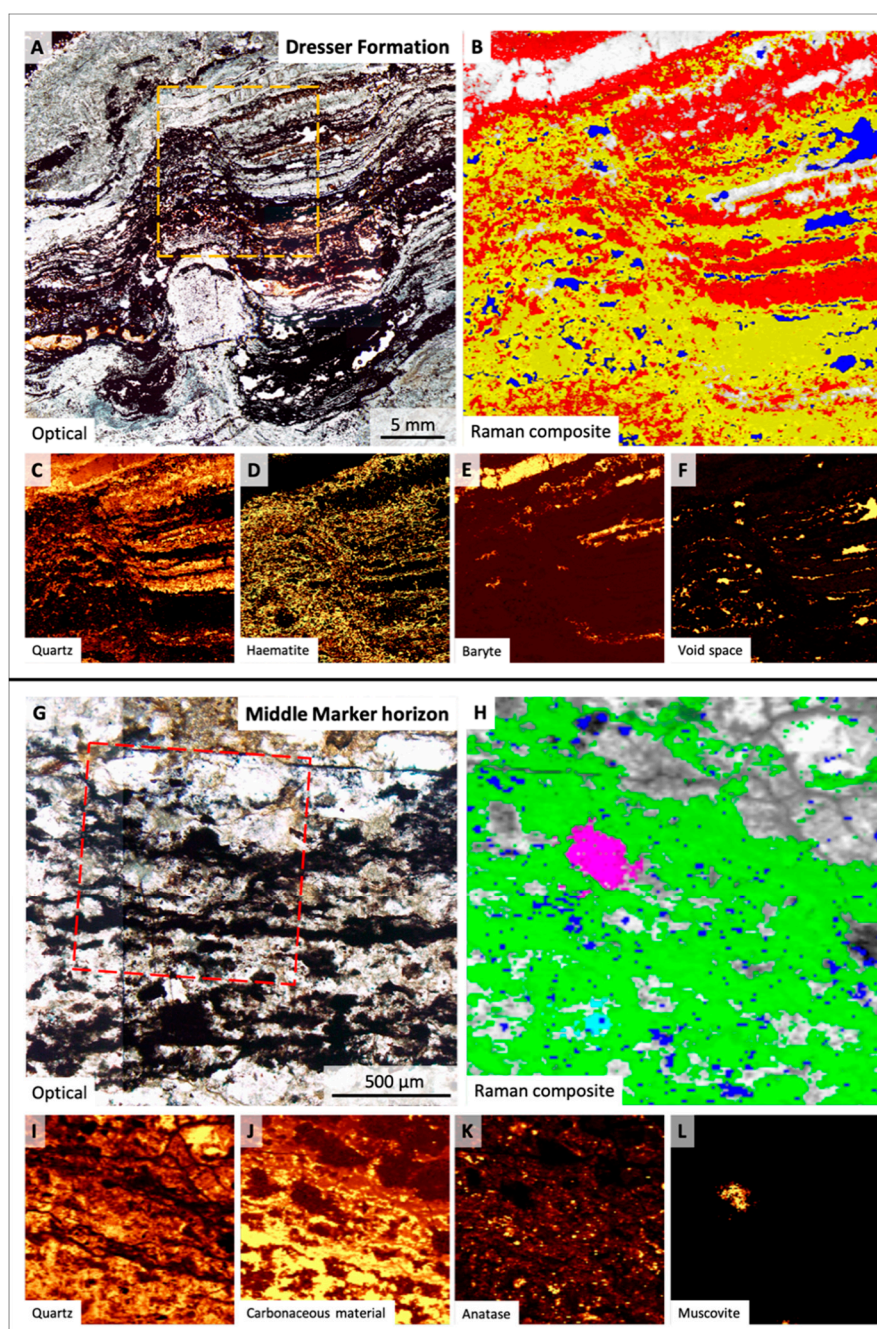


Figure 9. Raman spectroscopy mineralogical mapping of the two studied Precambrian samples. (A–F) Dresser Formation stromatolites (sample DF1). (A) Photomicrograph of the supra-lamina conical complexity analysed. Box indicates region of analysis. (B) Composite Raman map: yellow = haematite; red = quartz; white = baryte; blue = void space (araldite resin). (C–F) Raman heat maps for quartz, haematite, baryte, and void space. Scan parameters: objective Nikon E Plan 20 ×, 5 × 5 mm², 400 × 400 pixels (spectra), laser power 8 mW. (G–L) Middle Marker microbial mats (sample MM1). (G) Photomicrograph showing several microbial laminations in a coarse, sand-grade, silicified sediment. Red box indicates region of analysis. (H) Composite Raman map: grey = quartz; green = carbonaceous material; dark blue = anatase; fuchsia = muscovite; light blue = rutile. (I–L) Raman heat maps for quartz, carbonaceous material, anatase, and muscovite. Note the correlation of carbonaceous material with anatase. Scan parameters: objective Nikon E Plan 20 ×, 1.2 × 1.2 mm², 150 × 150 pixels (spectra), laser power 5 mW.

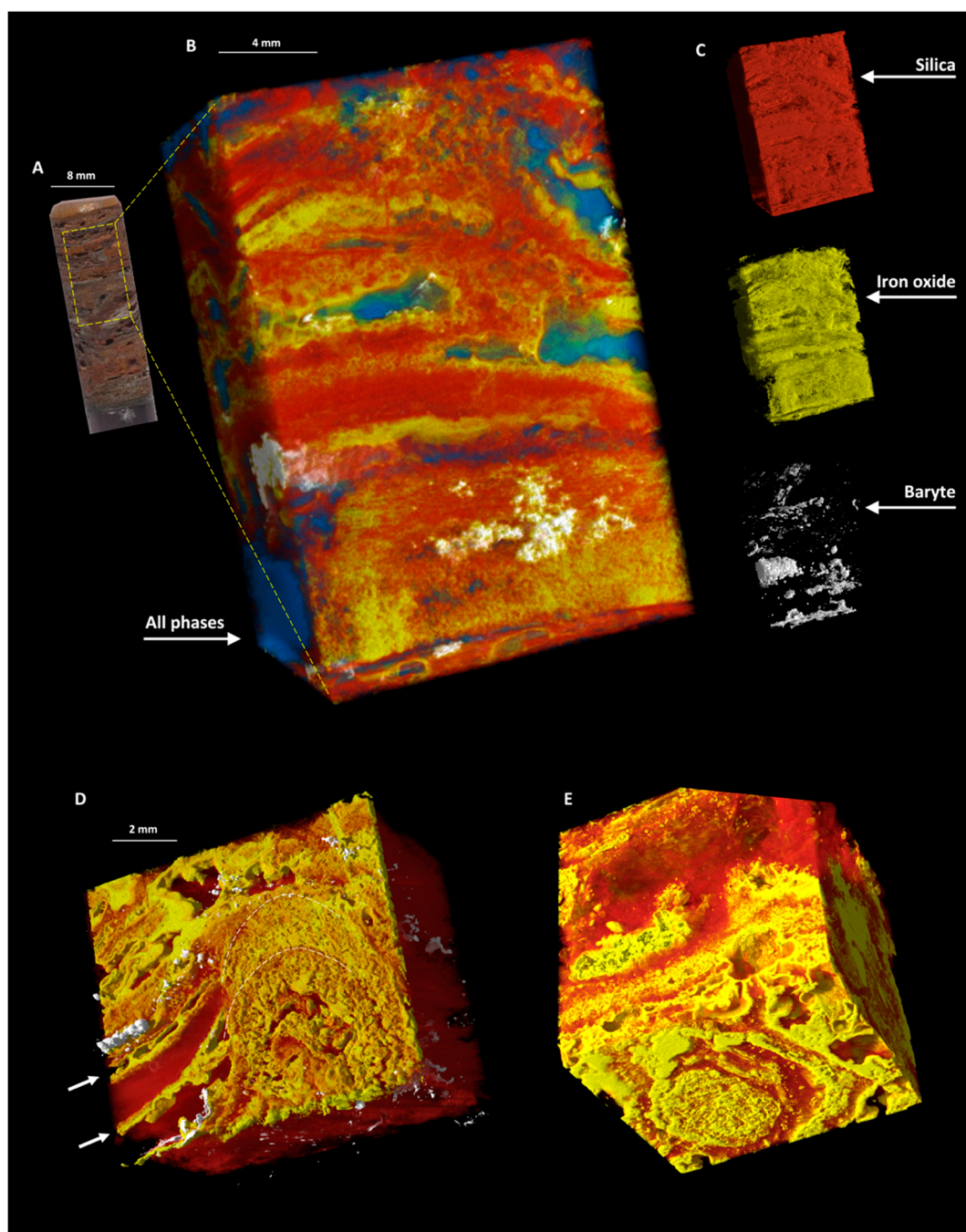


Figure 10. X-ray μ CT scan of a domical stromatolite from the Dresser Formation (sample DF1). (A) Photograph of the cylinder analysed. (B) Three-dimensional rendering: yellow = silica; red = iron oxide (haematite); white = baryte; blue = void space. (C) Distributions of the three mineral phases from the volume shown in B. (D,E) Tomographic reconstructions of two conical structures (supra-domical complexities) superposed on the limbs of the domical stromatolite. Morphological comparison can be made with the pinnacular microbial mat grown in a Cu-enriched medium (sample 805-Cu; Figure 5). White dashed lines indicate weak remnant laminations forming the silicified body of the dome. White arrows indicate haematite laminations forming poorly preserved revetment-like fabrics around the cone, analogous to those of the sheath-EPS-*Chloroflexus* layers surrounding the pinnacles of sample 805-Cu (Figure 5C–D). (E) Basal view of dome (circular cross-section visible). Conditions of acquisition: voltage = 120 kV; current = 150 μ A; frame acquisition time = 750 ms; views = 2000; pixel size = 3.86 μ m.

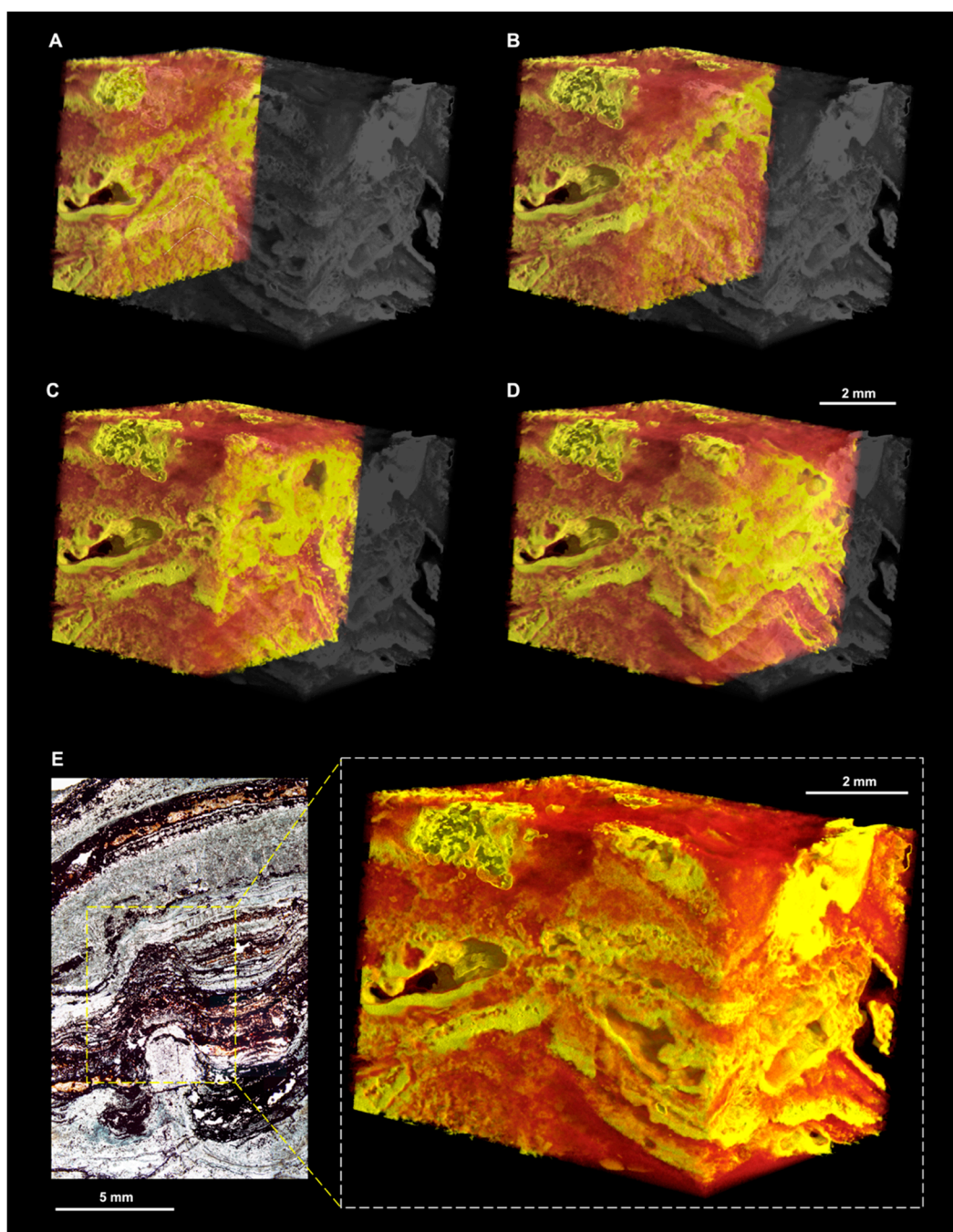


Figure 11. Tomographic reconstruction of a cone from the Dresser Formation stromatolite (sample DF1), using a cylinder cut from the sample corresponding to photomicrograph E. (A–D) Sequential reconstructions through the volume of the cone showing fabrics of interest: weakly laminated central region (dashed white lines in A) surrounded by a strongly laminated layer resembling the revetment layer in Figure 5C, and a fenestral cavity (void space). These scans clearly elucidate the three-dimensional lamina-specific characteristics of the stromatolite and the relationships of microfabrics that can be equated to those of modern microbialites. Ghost volume of the entire sample is shown on each scan to allow interpretation of microstructures within the macrostructure. (E) Whole volume scan of the cone shown in (A–D), directly compared with a photomicrograph of the conical-domical structure to which it corresponds. Conditions of acquisition: voltage = 120 kV; current = 150 μ A; frame acquisition time = 750 ms; views = 2000; pixel size = 3.86 μ m.

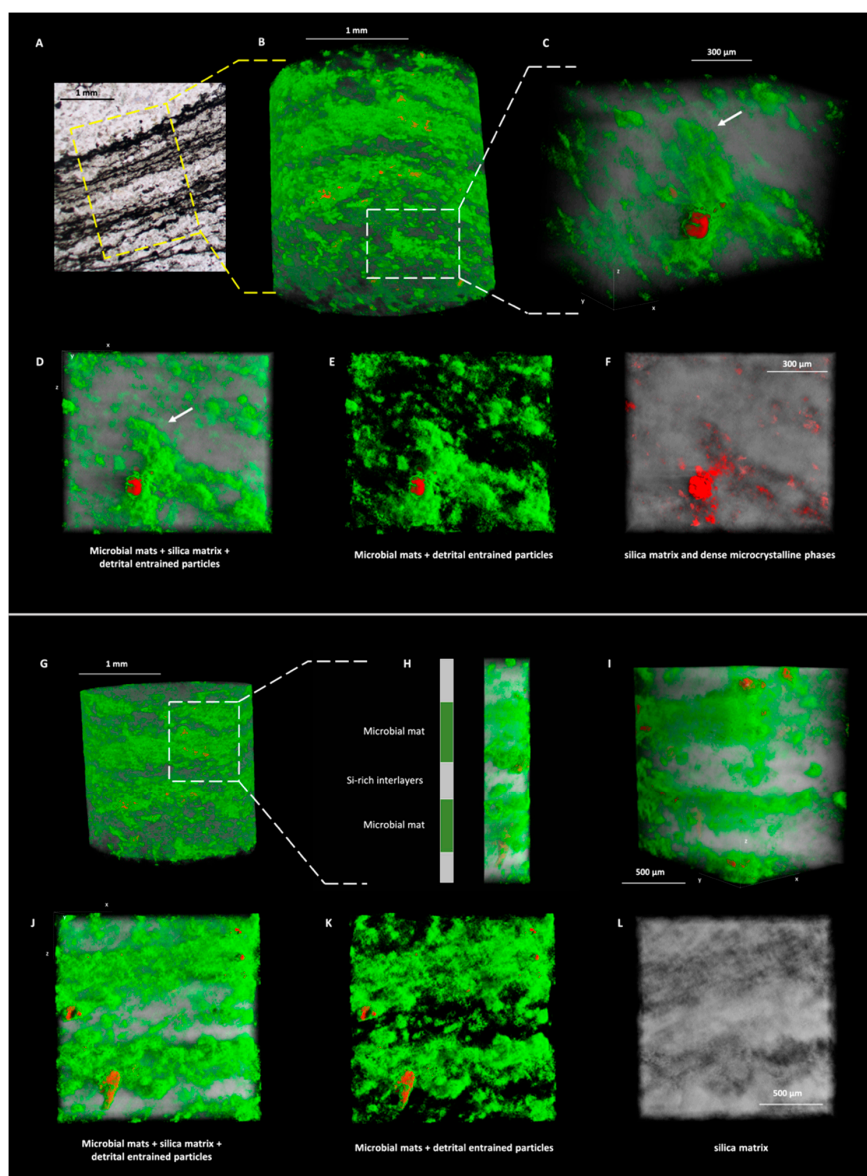


Figure 12. X-ray μ CT scans of carbonaceous laminations in a biolaminated sediment from the Middle Marker horizon (sample MM1). (A,B) Photomicrograph and X-ray μ CT scan of micro-tufted microbial mats. Yellow box in A indicates lamina stack equivalent to that shown in (B). White box in μ CT scan indicates sub-volume shown in (C–F). (C) Perspective view of sub-volume containing a $\sim 400\ \mu\text{m}$ tuft preserved in three dimensions (arrowed). Green = carbonaceous lamination; grey = silica matrix; red = denser phases. (D–F) Anterior views through the tuft (arrow in C equivalent to arrow in D). Note the association of denser material, resulting largely from anatase accumulation (see Figure 9K), with laminations (E,F). Note also the large red particle, which appears to be an equant grain bound by microbial filaments. (G) Sub-volume from the same cylinder comprising flat-laminated microbial mats (white box). (H) End view of the second sub-volume, distinguishing microbial mat laminations (green) and silica-rich interlayers (grey). Colour-coded column indicates layering. (I) Perspective view of the sub-volume showing the non-isopachous nature of the laminae. Red objects indicate denser phases entrained within the laminations. (J–L) Anterior views of the sub-volume showing the alternation of layers rich in carbonaceous matter and rich in silica. Phases are coloured consistently by density throughout the figure. Conditions of acquisition: voltage = 110 kV; current = 100 μA ; frame acquisition time = 1000 ms; views = 1800; pixel size = 1.19 μm .

3.1.2. PIXE

The results of two μ PIXE mapping experiments are presented here for comparative purposes, highlighting the elemental distributions in biological material in samples 805-Fe (Figure 4A,B) and 805-Cu (Figure 4C–E). In both cases, cellular material (both *Coleofasciculus* and *Chloroflexus*) is broadly associated with enrichments of K, Na, Mg, S, and P. In sample 805-Fe concentration, Fe is dispersed throughout biological material such that it appears negligibly concentrated and does not visibly correlate with other elements, only within minor oxide particles attached to microbial filaments (Figure 4B). PIXE element maps from 805-Cu present a different scenario. In the studied mat fragment, Cu, Mn, and Fe are concentrated in the upper layers at the base of the pinnacle (the top of the mat; Figure 4E) which, according to SEM imagery, corresponds largely to the exuded exopolymers and the empty sheaths of *Coleofasciculus* (Figure 2H–K), i.e., a region of reduced *Coleofasciculus* biomass and increased *Chloroflexus* biomass. There is a negative correlation between the association K–Na–Ca–Mg–S–P in biomass beneath the upper polymer-rich layer and the association Cu–Mn–Fe in the polymer-rich layer (Figure 4E). In contrast to 805-Fe, Fe and Mn are located almost exclusively in the upper tens of micrometres and are not dispersed throughout the volume of the mat.

3.1.3. X-ray μ CT

Fragments from samples 805-Cu and 1011—the two samples exhibiting surface relief in the form of pinnacles or tufts—were analysed using X-ray μ CT with the objective of detecting 3D morphological features not observable by optical microscopy or SEM. Sample 805-Cu was studied by μ CT at a pixel size of 6.87 μ m. Carefully separating the higher and lower density pixels corresponding to the microbial material delineated sequences of alternately dense and less dense laminations composed of filamentous material (Figure 5B,C). Achieving this density delineation relies on iterative separation of higher and lower values in the histogram peak corresponding to biological material in VG-Studio Max software. This distribution directly echoes combined SEM and μ PIXE observations, which distinguished *Coleofasciculus*-rich underlying laminations (Figure 2L) overlain by laminations comprising discarded sheaths, EPS, and *Chloroflexus* (Figure 2H–K) with differential enrichment in heavy metals (Cu, Fe, Mn) after growth experiments (Figure 4E). In μ CT renderings, *Coleofasciculus* (dominant in terms of biomass) is rendered in green (less dense; Figure 5) and sheath-EPS-*Chloroflexus* layers incorporating heavy metals are rendered in red (denser; Figure 5). Consistent with μ PIXE scans, all cellular material incorporates a range of lower atomic number elements (K–Na–Ca–Mg–S–P), but there is a strong enrichment of heavier Cu, Mn, and Fe in the upper layers. The large pinnacle itself is also dominantly composed of *Coleofasciculus*-rich biomass (Figure 5B), further corroborating SEM observations (Figure 3) and suggesting that *Coleofasciculus* is the architect of large, pinnacle-like surface convexities. μ CT scans reveal that the pinnacle-covering revetment shows different filament orientations (mostly horizontal; Figure 5D) and a density consistent with sheath-EPS-*Chloroflexus* biomass. This revetment is thin and discontinuous, becoming increasingly patchy toward the top of the pinnacle (Figure 5B), suggesting that its formation is a consequence of pinnacle growth, i.e., *Coleofasciculus* forms the pinnacle while the *Chloroflexus*-rich layer either follows pinnacle growth or is disrupted by it, confirming the 3D distribution of biomass observed in Figure 3A–C. The two communities form a supra-lamina convexity (the pinnacle) that preserves two fabrics rendered with high fidelity using μ CT (Figure 5D):

- An interior fabric with domains of both horizontally laminated and randomly oriented filaments of homogeneous size, wherein the degree of randomness in orientation increases with height; and
- An exterior revetment of mostly vertically oriented filaments with a bimodal size distribution (some very fine, some thick).

A representative tuft from sample 1011 was also analysed using μ CT at an almost identical pixel size of 6.88 μ m. In contrast to sample 805, the biomass was homogeneous (not stratified) and exhibited neither alternating lamination densities, nor a dense revetment surrounding the tuft-like convexity (Figure 6C). This is consistent with SEM images of a well-mixed community throughout (Figure 3D–J).

Denser particles occur both within the tuft and at its peak (Figures 3D and 6D), but are gypsum and celestine (XRD and EDS analyses, not shown), which had precipitated as a result of evaporative processes. Contrary to the pinnacles of sample 805-Cu, the tufts in sample 1011 did not produce textural divisions that are visible in μ CT, nor intimate micromorphological relationships between biomass (Figure 6C–E). Crucially, this comparison demonstrates that differing geochemical stresses do not necessarily produce convergent micromorphological expressions. It is thus reasonable to use only *detectable* micromorphologies as a morphogenetic tool to explain the origins of fossil OSS under the assumption that remnants of these micromorphologies may be preserved in the fossil record. This comparison is made in Section 3.2.

3.2. Precambrian Samples

3.2.1. Petrographic Characterisation

Domical–conical stromatolites from the Dresser Formation (sample DF1) exhibit convexities on the scale of millimetres to centimetres (Figure 7). Sampled stromatolites have a laminar–domical macrostructure, and supra-laminar micromorphologies (in this case, supra-domical complexities with conical forms). In other words, the laminations forming centimetre-scale domical structures (the macrostructure; Figure 7E,F) also form irregular conical complexities that rise out of individual domes. Thin section observations show that laminae are non-isopachous, i.e., of inconsistent thickness throughout three dimensions, and are punctuated by fenestrae (Figure 7A–D). Raman spectroscopy shows that the stromatolites comprise silica (SiO_2), baryte (BaSO_4), and haematite (Fe_2O_3) (Figure 9A–F), three minerals that may be easily separated in μ CT due to their density differences (2.65, 4.48, and 5.24 g cm^{-3} , respectively). Together with fenestrae, which are either voids or poorly silica-infilled spaces, the relationships between all phases may be easily reconstructed in three dimensions. The Dresser stromatolites thus make ideal candidates in which μ CT may resolve lamination-scale features indicative of biological processes. The ease with which one can analyse individual laminations in 3D enables direct comparison with the μ CT scans of samples 805-Cu and 1011, which have superficially similar topography. Furthermore, modern and Precambrian samples are often of similar dimensions and, if formed by similar microbial consortia (phototrophs including cyanobacteria and/or anoxygenic photosynthesisers), may enable ecophysiological morphogenetic comparison.

Micro-tufted microbial mats from the Middle Marker horizon (sample MM1; Figure 8) present a complementary case. These laminations occur in fine-grained silicified sediments, and feature tufts around $100 \mu\text{m}$ in size [7], similar to microbial structures from the Dresser Formation [45]. Raman spectroscopy identifies three major phases (the silica matrix, laminated carbonaceous material, and anatase) and two minor phases (muscovite and rutile), the latter occurring as isolated grains (Figure 9G–L). The petrological context of these microbial mats presents a challenge for μ CT, since the atomic masses of C and Si—the dominant phases in the structure and matrix—are very similar. Raman spectroscopy indicates that TiO_2 (anatase) co-occurs with laminated carbonaceous material (Figure 9K), which may ease the visibility of laminations in μ CT renderings.

3.2.2. X-ray μ CT

Sample DF1 has a domical–conical macrostructure (Figure 10A,B) composed of three variably dense phases that can be readily extracted in volumes of stromatolite DF1 (Figure 10C), corresponding to silica, baryte, and haematite (red, yellow, and white in Figure 10). The sample also includes a large volume percentage of fenestral void space (blue in Figure 10B, arrowed in Figure 11). Three cone-like microstructures (supra-domical complexities) were identified within the scanned volume and analysed using μ CT (Figure 10D–F and Figure 11). These conical micromorphologies preserve two fabrics:

- A poorly preserved, less dense (red–yellow, i.e., mostly silica) interior fabric with mostly randomly oriented structure. The central region has weak remnant lamination (dashed white lines in Figures 10D and 11A); and
- An exterior fabric of thicker laminations overlying the interior fabric, producing a revetment of slightly higher density (yellow–red, i.e., mostly haematite; arrowed in Figure 10D).

Sample MM1 presents a different case. The association of carbonaceous material with anatase allows the clear distinction of the microbial mat in three dimensions. Three phases can be distinguished in our X-ray μ CT scans:

- The silica matrix (grey in Figure 12), which is present throughout the entire sample volume;
- Carbonaceous material (green in Figure 12), enriched in microbial laminations; and
- Denser phases (red in Figure 12) corresponding to anatase associated with the microbial laminations and altered volcanic particles and unsilicified particles, both entrained within the laminations and scattered throughout the matrix. Dense particles are sometimes surrounded by filament-like carbonaceous material (arrowed in Figure 12).

X-ray μ CT of sub-volumes from the analysed cylinder illuminates the non-isopachous character of the laminations (Figure 12B,G), demonstrates the ubiquitous silicification of the sample (Figure 12F,L), and illuminates the microstratigraphy within individual lamina sets (e.g., Figure 12H). It is not, however, possible to distinguish interior and exterior fabrics within these smaller-scale convexities. The microbial laminations comprise carbonaceous material and microcrystalline silica, the latter being the preservational agent and the overwhelmingly dominant matrix component.

4. Discussion

4.1. Comparative Morphogenesis in Modern and Ancient Microbialites

The following provides a summary of the results obtained, together with potential implications:

- Microbial mat communities grown in the presence of enriched concentrations of toxic Cu (sample 805-Cu) formed surface convexities (microstructures), termed pinnacles, atop their macrostructure (Figures 1 and 3). Pinnacles did not develop in the presence of other metal enrichments (Fe, Ni, Mn, and Sr were tested; Fe results shown (sample 805-Fe) in Figure 4A). We thus infer a cause and response relationship between elevated Cu concentrations and the development of surface convexities. Phototaxis can be excluded as the driver of pinnacle growth, as the light intensity at the surface of the mats was homogeneous.
- SEM imaging (Figures 2 and 3) and μ PIXE elemental mapping (Figure 4) demonstrate that the community forming both the mat and pinnacles (*Coleofasciculus*–*Chloroflexus*) appears to stratify into two distinct layers in the presence of Cu (Figure 5D). The first is an inner *Coleofasciculus*-rich layer which exhibits some laminated micromorphology, and the second is a thin sheath-EPS-*Chloroflexus* layer (Figures 2 and 3) forming a sparse revetment on and between the pinnacles (Figure 5). This spatial segregation (the inverse of that in the 805 field sample) occurs as a function of organismal tolerance to Cu, i.e., *Chloroflexus* is Cu-tolerant, whereas *Coleofasciculus* is intolerant to Cu and retreats to the interior, producing EPS and discarding sheaths in the outer layer (Figure 2H,I).
- Since heavy metal enrichments (Cu, Fe, Mn) give rise to density contrasts, X-ray μ CT can corroborate this morphogenetic process, detecting the slight density differences between the denser sheath-EPS-*Chloroflexus* layer and the less dense *Coleofasciculus* layer (Figure 5), consistent with the binding of heavy elements in the former. Although only Cu is toxic, its sequestration co-locates with Mn and Fe, suggesting that the exuded EPS is non-specific in its capacity for metal binding (see [14,46]). (Figure 4E). Fe and Mn are not toxic to either of these organisms, but their downward diffusion is nonetheless limited by the ecophysiology of the microbial

consortium. μ CT shows that *Coleofasciculus* is the architect of the pinnacles, which grew out of the *Coleofasciculus* layer beneath (Figure 5B,E), consistent with its enhanced response to Cu toxicity. Pinnacle formation is thus a mitigation of toxicity stress. X-ray μ CT also discerns the textures of density-distinct layers: horizontally and randomly oriented filaments in the inner region and vertically oriented filaments in the revetment (Figure 5).

- (iv) Although microbial mats from the same sampling locality and with the same initial community composition can develop superficially similar pinnacle or tuft-like morphologies in the presence of different geochemical stressors (i.e., toxic elements for samples 805-Cu and increased salinity for sample 1011), not all forcings create micromorphological features that can be distinguished by tomography and used as interpretative tools for fossil OSS morphogenesis. X-ray μ CT cannot resolve density contrasts where no such contrasts exist, as in sample 1011 (Figure 6C) which, despite having experienced salinity stress, has not segregated its community (Figure 3D–J). Ergo, reactions to geochemical stresses may or may not bestow upon the geological record a detectable 3D morphology from which the causal stressor in a fossil example could be determined. Unlike many conical OSS, the supra-lamina complexities studied herein are not exclusively biophysical responses, but result from interactions with the environment over small temporal and spatial scales [25,30].
- (v) X-ray μ CT scans of two Precambrian OSS—samples DF1 and MM1—show that these ancient microbialites exhibit 3D characteristics that echo those in samples 805 and 1011. The comparison is particularly close, despite some recrystallisation, in the case of the Dresser Formation domical–conical stromatolites (DF1) and sample 805-Cu. Both feature two-layer microstructures consisting of a poorly laminated central region (the cone/pinnacle) surrounded by a revetment. The Middle Marker mats (MM1), contrastingly, can be compared qualitatively to sample 1011, but it is difficult to make conclusive statements concerning their morphogenesis, since the modern process analogue sample 1011 did not exhibit induced micromorphologies resulting directly from salinity stress.
- (vi) Both modern and Precambrian OSS exhibit multi-scale topographic complexities, e.g., pinnacles and cones atop flat-lying, undulating, or domical macrostructure. Morphologies in modern samples studied by μ CT (pinnacles, cones and tufts) are supra-lamina complexities resulting from geochemical stresses over short timescales. These millimetric features, superimposed upon the macrostructure, may reflect either what Petroff et al. [30] called “growth in a randomly fluctuating environment” or intrinsically stochastic processes resulting from biofilm-scale complexities, for example, biofilm roughness, surface fractal dimension, biofilm compactness, and interior transport potential [47]. Similar structures in ancient OSS may be interpreted as having an equivalent morphogenesis.

It is thus possible to make a comparison between the modern and ancient OSS studied in terms of pulsed growth in response to a changing environment. In the following, we focus on biophysical and ecophysiological processes, parameters and models that might further substantiate this idea, and assess the potential of interpreting Precambrian OSS using modern microbialites as process analogues. This will aim to answer: (i) to what extent are palaeoenvironmental characteristics reflected in micromorphological signatures, and how might these signatures be observed using three-dimensional correlative microscopy? and (ii) can detectable features at the scale of individual laminations confirm the morphogenesis (and therefore biogenicity) of ancient OSS in the absence of microfossil preservation?

4.2. Three-Dimensional Morphogenetic Biosignatures

Microbialite growth is governed by a wide range of parameters relating to community composition (intrinsic) and the external environment (extrinsic), each of which leaves deducible traces in the structure (Figure 13). Comparing modern and ancient OSS to identify microstructural similarities meets the challenge of stromatolite ‘bioconfusion’ raised by Awramik and Grey [10]: that we should be able to make estimations of biogenicity in controversial ancient stromatolites based on uniformitarian

comparisons against modern stromatolites, however, we will fail to do so for as long we lack a unified morphogenetic framework. Mathematical modelling of stromatolite growth based upon observations of natural samples, as outlined in Section 1, has been crucial in parameterising morphogenetic processes. The definitions of the terms of each equation provide a means of predicting the eventual morphologies of OSS, and mismatches between expected and measured morphologies identify inconsistencies requiring explanation [36], which may be biological.

In vivo, the biogenetic processes in microbial biofilms are governed by the production of autoinducer molecules that interact with biofilms and control their interactions with the environment as a function of local cell-population densities [26,31,48,49]. Autoinductive signalling is strongly linked to the concentration of quorum-sensing bacterial cells, and controls phenotype expression, for example, the formation of biofilms after the adhesion of members of the community onto one another through the production of a matrix of extracellular polymeric substance (EPS) [50]. Although many functions of EPS are speculative [31], it certainly functions as a structural entity [51] and as one part of the external environmental compartment of the metallome [52,53], which is to say that it supports the biofilm and hosts both sequestered metals and extracellular metalloenzymes within the biofilm microenvironment [14,50,54–56]. Carboxyl residues of peptidoglycan and teichuronic and teichonic acids within the cell wall, proteinic outer-membrane lipopolysaccharide polymers (and capsules where present), such as carboxylate (alduronate and pyruvate), hydroxyl (tridentate), sulfates, and amine groups are active sites of metal sequestration [53,54], and may account for the aggregation of microbe-metal signatures [57,58]. This immobilised metallic signature, the cell-associated metallome, may also leave an imprint in the fossil record [57,59], since it is difficult to resolubilise metal out of specific organic sinks, such as bacterial cellular products, which tend to outcompete other chemicals in natural systems in terms of metal retention [55]. Although metallic elements serve essential functions to most bacterial metabolic pathways [60–62], many—including Fe, Ti, Zn, Cu, and As—are toxic to certain microbial strains and communities. When toxic metals are enriched in the local environment, induced production of EPS and modification of the immediate environment has often been observed as a mechanism to sequester these elements [63–65]. This may be particularly necessary at the interface between microbial mats and the overlying water column, since the basal millimetres of the medium are characterised by laminar, poorly mixed flow [31] in which toxic elements may become concentrated. This situation resembles the aquaria studied herein, where Cu- and Fe-enriched waters remained in contact with the growing mat, and a response to toxicity was observed: the volume of EPS at the surface of sample 805-Cu (Figure 2G–L) is far greater than at the surface of sample 805-Fe (Figure 2A–F). This environmentally driven phenotypic modification to sample 805-Cu accompanies ecosystem restructuring and results in non-specific metal-binding by EPS, demonstrated by correlated SEM imaging, PIXE elemental mapping, and μ CT three-dimensional reconstruction. EPS, abandoned cyanobacterial sheaths, and Cu-tolerant *Chloroflexus* are spatially correlated with enrichments in heavy elements (Fe, Mn, Cu) in the upper region of the mat, making possible their distinction in 3D scans. Neither SEM imaging nor X-ray μ CT scanning of sample 1011 show density- or orientation-distinct microfabrics, but rather a well-mixed community throughout the tufts. This is most likely because salt stress does not adversely affect either of the members of the community, but is possibly due to perturbation of the surficial layer by osmotic pressure. The phenotypes exhibited by samples 805-Cu and 1011 are therefore distinct and that of 805-Cu is morphogenetically explicable through biological interaction with the environment.

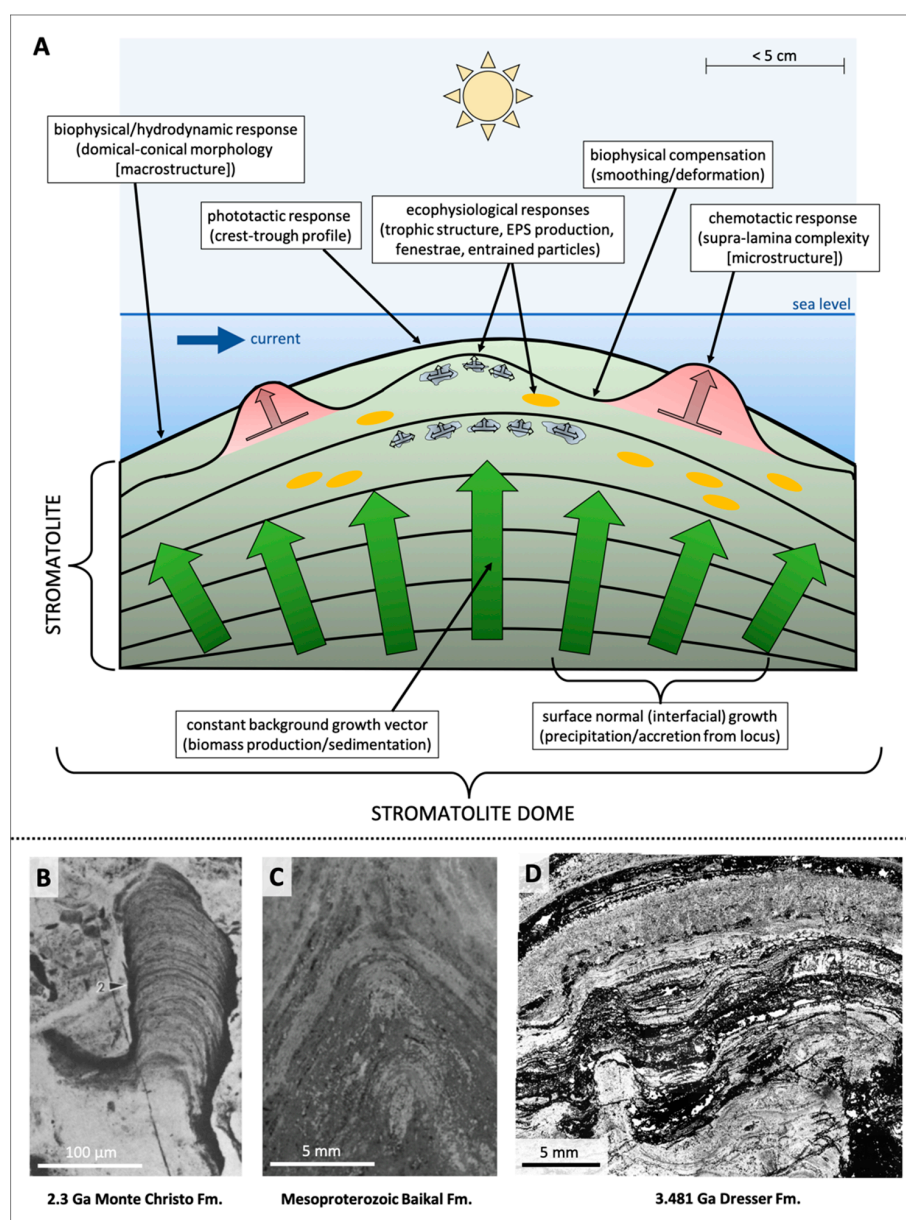


Figure 13. Synthesis of our approach to the mechanistic morphogenesis of organo-sedimentary structures growing under geochemically stressed conditions, with relevant examples from the geological record. The growth vectors considered are those evoked in the mathematical models described in Section 1, such that this schematic might be used as a means of predicting stromatolite morphology, or retrospectively resolving misfits in observed morphology with model predictions. (A) Schematic growth model highlighting ecophysiological, biophysical, and hydrodynamic processes involved in stromatolite growth, together with resulting macroscopic and microscopic morphologies. (B–D) Three examples of topographic complexities in stromatolites from the geological record. The morphology of B is dominated by phototactic processes and surface normal growth, producing recognisable overhangs. C is controlled by surface normal and phototactic processes, with considerable ecophysiological contributions (non-isopachous laminae, fenestrae) providing distinctive evidence for biology. D, as described herein, is a more complex morphology characterised by phototactic, surface normal, and ecophysiological (particularly EPS production and trophic structuring) processes, upon which is superimposed evidence for chemotactic forcing on short timescales. Mesoscopic study of stromatolite morphology (e.g. Petroff et al. [29,30]) and outcrop study of centimetre- and metre-scale stromatolite reefs (e.g., Hofmann et al. [2]) could underpin the significance of microscopic, lamina-scale characteristics (this study).

Since chemical diffusion through the mat is greatest at regions of high curvature [29,30], increased EPS production in surficially complex structures in the presence of stress should contribute to increase their surficial complexity. EPS production is thus a morphogenetic and morphological parameter that is driven by both intrinsic biological and extrinsic environmental factors. We tentatively suggest that this process is a candidate process for quantifying the random noise parameter of the KPZ equation, and that the produced morphology is a definitively biological microstructure: EPS- and sheath-rich layers, i.e., with extracellular contributions from both *Coleofasciculus* and *Chloroflexus*, surrounding biomass-dominated layers. Attempts to model the fit of microbialite growth in environments stressed by variable concentrations of biotoxic elements would be a promising means by which to confirm such geochemical stress as a driver of morphological complexity. Future modelling efforts, taking into account differential microbial responses to an applied stress field, may enable the small scales at which models are no longer applicable due to increased contributions from ‘noise’ to be quantified. Since EPS has a high potential for fossilisation [17,66], a surficial complexity of small scale (pinnacle/cone/tuft) may be exceptionally preserved in the fossil record as a biologically indicative, macroscopically visible structure, as shown herein (Figure 7, Figure 8, and Figure 13). The pinnacles observed in 805-Cu are identifiable, discordant features at the scale of an individual lamination with spatial orientations perpendicular to the main body of the mat (Figure 5C). The main body of samples 805-Fe and 805-Cu is a gently undulating, flat-laminated structure with mostly horizontal fabric and textural elements; however, this flatness may simply be a representation of the hydrodynamic stillness of the mat growth experiments relative to natural conditions; a repeating domical structure is more likely in hydrodynamically active environments [4,29]. Fabric elements within pinnacles trend in multiple orientations: the *Coleofasciculus* interior is horizontally laminated, whereas the exterior EPS-sheath-*Chloroflexus* revetment is essentially vertically laminated (Figure 5C). This micromorphological parallel between the pinnacles of sample 805-Cu and the supra-domical structures of sample DF1 allows us to advocate the biogenicity of the latter controversial Archaean structures in light of modern examples. In contrast to previous estimates of their biogenicity, which have relied on characteristics of the macrostructure [40,67] and microfossil-like objects of unclear affinity [68], we have provided herein a mechanistic interpretation of the micromorphology of these Dresser Formation stromatolites with reference to a well-characterised process analogue (sample 805-Cu). Our reasoning is logically consistent with that when ancient OSS are essentially identical to younger OSS, similar processes and forcings were likely involved in their formation [10]. We advance the suggestion of Cuerno et al. [36], providing a mechanistic demonstration of a biogenic origin for structures that are not readily explicable through the terms defined by mathematical morphogenesis at small scales. A brief literature survey shows that such ‘unpredictable’ complexity is common in contemporaneous and younger stromatolites of biological origin (e.g., [67–72]), but is not present in stromatolite-like structures of more likely abiological origin [73–75], where the eventual morphologies and, indeed, a dominantly phototrophic affinity, can be predicted in terms of either KPZ or diffusion-limited dynamics alone. Given the valid application of KPZ, DLA, and DLA-CA models to OSS of varying morphology, the specific model required for morphogenetic studies of Precambrian OSS must be determined on a case-by-case basis, considering the petrological context given by correlative biogeochemical analyses.

Microbialite macrostructure is a function of particle accretion, hydrodynamics, and competition, irrespective of internal complexity [19,29,30]. This is corroborated by the 3D analyses shown herein, but bulk morphology (the macrostructure) does not seem able to unambiguously prove biological origin [4,21]. We propose that supra-lamina morphological complexities comprising the microstructure, in contrast to the macrostructure, may be demonstrated as being exclusively biogenic within the framework shown in Figure 13. Strategies of resilience to environmental stress, e.g., metal immobilisation, may give rise to multi-layer heterogeneous micromorphologies discernible by X-ray μ CT at the scale of individual laminations. This allows an interpretation of DF1 stromatolites based upon the *morphogenesis* of the modern 805-Cu. Sample MM1, although exhibiting morphological parallels with sample 1011—for example, a homogeneous laminated structure entraining dense,

suspended particles and tuft-like surface morphologies—does not preserve morphogenetically diagnostic textures, thus no mechanistic interpretation can be made regarding sample MM1 based on sample 1011. Tufted and reticulate mats such as these have been ascribed passive origins unrelated to stressed environments, for example, the gliding motility of certain bacteria that causes reticulate structures to build after the collision, alignment, and clumping of cells [76], or generalised behavioural processes in mat-building organisms with specific morphologies, such as sheathed filamentous microbes [77]. Such processes are potential candidates for the formation of micro-tufts in the Middle Marker mats, and do not require specific geochemical scenarios. Regrettably, the approach developed herein does not allow us to distinguish whether such processes played a part in the morphogenesis of the studied tufted and micro-tufted microbialites.

Supra-laminar surface complexities are short-term growth phenomena likely preserved only in rapidly mineralised OSS, such as the silicified examples shown herein. In the Precambrian examples studied, the agent of preservation is silica, which was highly concentrated in the Archaean oceans as a consequence of the alteration of bedrock lithology, a lack of biological sinks, and Si-rich hydrothermal effusions. Where such exquisite preservation is achieved, the three-dimensional correlative microscopy approach applied herein may assist in the determination of the origins of the structures and the correct morphogenetic model for understanding putatively biogenic fabrics within OSS. Furthermore, correlative microscopy may distinguish indications of biological interaction with the palaeoenvironment in the oldest traces of life on Earth. Microstructures with predictable biogenic origins should be considered strong morphological biogenicity criteria. In conclusion, 3D microstructures exceptionally preserved in ancient OSS may record short-term snapshots of the interactions between palaeobiology and palaeoenvironment. Such bio-indicators as analysed herein circumvent the issues inherent in proving biology based only on *morphology*, since such structures uniquely prove biology based on *morphogenesis*. Morphogenetic bio-indicators should be considered a keystone to demonstrating the biogenicity of fossil OSS at the scale of individual laminations.

4.3. Morphogenesis Reflecting Evolutionary Strategies Through Time

Have tolerances to elements changed over geological time in different microbial phyla? Differences in the magnitude of response to stressors and the temporal change in OSS morphologies throughout geological time (e.g., conical-domical Archaean forms versus dendritic Proterozoic forms) remain questions to be solved, but are potentially linked to evolutionary processes. Grotzinger and Knoll [22], for instance, noted that whereas Archaean stromatolites appear to accrete mostly by lamina precipitation and preservation, Palaeoproterozoic and younger forms develop mostly *via* carbonate precipitation. In these two Era-defined groups of OSS, the magnitudes of certain terms in morphogenetic equations would be very different, implying a differing balance between intrinsic and extrinsic factors. The vast record of OSS with varied morphologies but similar structural elements (laminations, biominerals, bound particles, carbonate precipitation; Figure 13) is evidence that they develop through a class of common morphogenetic processes producing a suite of diverse structures.

The timescale of growth of a biofilm is estimated at days to weeks [9,29] and most fossil biolaminites and individual stromatolitic lamina therefore represent weeks to months of growth. Precambrian OSS can be classified either as stage 2 or stage 3 developing and climax consortia [3,8,9], and therefore once hosted trophic stratification, although this biological diversity is seemingly not preserved in the fossil record. The laminations inherent to all classes of OSS represent brief moments in geological time. The relationships between organisms with varying tolerance to certain geochemical stressors could form a part of the morphogenetic processes responsible for short-term pulsed and cyclical changes of shape and form in Precambrian fossil OSS. While hydrodynamic (abiotic) factors define the macromorphology of OSS, short-term environmental stressors can cause the development of demonstrably biosynthetic micromorphological peculiarities (e.g., pinnacles in sample 805-Cu) that do not follow the trends of structural elements in the macrostructure. Although one can only speculate on the differences in community composition between microbial mats and stromatolites in deep time, we note that since

Archaean habitats would have contained higher concentrations of many metal and metalloid elements due to widespread volcanic activity and hydrothermal fluxes [78,79], the morphological response to such enrichments at the scale of individual laminae should be more pronounced if communities exhibited similar responses then and now. Growth experiments show that mat-building consortia are capable of producing centimetric morphological responses to stress, but the consortia involved in the experiments presented herein (and indeed all other experiments with similar goals) are not necessarily direct analogues of Archaean communities, e.g., they include cyanobacteria, for which there is no compelling evidence before 2.7 Ga [11,80]. Furthermore, metallic elements that are nowadays recognised as toxic often form an integral part of the metabolic machinery of anaerobic prokaryotes [60,81], which were common mat-builders in the Archaean [11,13]. The changing role of metals through geological time and their gradual incorporation or exclusion from the enzymes governing primary benthic productivity may have influenced microbial mat architecture over hundreds of millions of years. Morphological differences in OSS through time therefore represent, at the lamina-scale, either or both of (i) differential exposure to ambient fluids enriched in toxic elements at the time of growth, and (ii) changing tolerances to toxic elements through geological time, as the loci of primary productivity shifted from anaerobic to aerobic photosynthesisers.

5. Conclusions

The modern and Precambrian examples analysed herein teach several lessons for the interpretation of OSS morphogenesis in two and three dimensions. Where modern process analogues producing micromorphologies under certain experimental stresses yield 3D textural distinctions matching the micromorphologies of Precambrian structures, we propose that the former may be used as an interpretative framework for the latter. This provides a *morphogenesis*-based proof of biogenicity for ancient OSS, and overcomes the issues inherent in the proof of biogenicity based only on morphology, since morphology may result from either biological or abiological processes. Where modern process analogues do not produce distinct micromorphologies, even in macromorphologies that grow under explicit ecophysiological stress, they should not be invoked as interpretative frameworks for Precambrian examples. Mechanistic palaeobiological interpretations based on morphogenesis are potentially powerful tools for determining the biogenicity of fossil OSS, but must be applied with caution. Using this rationale, we have demonstrated that stromatolites from the Dresser Formation may be deemed biological based on 3D morphologies tied to morphogenesis; however, microbial mats from the Middle Marker horizon require further evidence to determine their intrinsic ecophysiological growth processes. Morphologies of OSS that cannot be predicted by mathematical modelling (e.g., overhangs, supra-lamina complexities, localised fenestral cavities) should be considered indicative of microbial processes. Supra-lamination complexities, as defined and described herein, are lamina-scale features that develop on short timescales in response to local geochemical stress and are a product of unpredictable growth. They may prove stromatolite biogenesis in the absence of microfossil preservation. Since microfossils are very rarely preserved in Archaean stromatolites, the burden of proof for stromatolite biogenicity usually falls upon characteristics of their laminations.

Although morphological similarity between two laminated structures is not sufficient evidence to draw a direct palaeobiological parallel between them, it is consistent with the structures having similar *morphogenesis*. The study of OSS in deep time must be conducted at multiple scales in two and three dimensions within the morphology of the structure (Figure 13), and the interpretation of such structures is greatly assisted by microbial growth experimentation and modelling considerations. When unexpected morphologies can be explained using observed growth phenomena (*morphogenesis*) in modern process analogue microbialites, the case for the biogenicity of ancient OSS is significantly strengthened and processes generating their morphologies may be inferred. Archaean microbialites rarely yield diagnostic evidence of the organisms responsible for their formation, but understanding the processes involved in their co-evolution with the palaeoenvironment may yet illuminate some aspects of their biogenesis. The wide range of OSS morphologies observed throughout the geological

15. Gautret, P.; De Wit, R.; Camoin, G.; Golubic, S. Are environmental conditions recorded by the organic matrices associated with precipitated calcium carbonate in cyanobacterial microbialites? *Geobiology* **2006**, *4*, 93–107. [\[CrossRef\]](#)
16. Doemel, W.N.; Brock, T.D. Structure, growth and decomposition of laminated algal-bacterial mats in alkaline hot springs. *Appl. Environ. Microbiol.* **1977**, *34*, 433–452.
17. Tice, M.M.; Lowe, D.R. The origin of carbonaceous matter in pre-3.0 Ga greenstone terrains: A review and new evidence from the 3.42 Ga Buck Reef Chert. *Earth-Sci. Rev.* **2006**, *76*, 259–300. [\[CrossRef\]](#)
18. Homann, M.; Heubeck, C.; Airo, A.; Tice, M.M. Morphological adaptations of 3.22 Ga tufted microbial mats to Archean coastal habitats (Moodies Group, Barberton Greenstone Belt, South Africa). *Precambrian Res.* **2015**, *266*, 47–64. [\[CrossRef\]](#)
19. Hofmann, H.J. Stromatolites: Characteristics and utility. *Earth-Sci. Rev.* **1973**, *9*, 339–373. [\[CrossRef\]](#)
20. Verrecchia, E.P. Morphometry of microstromatolites in calcrete laminar crusts and a fractal model of their growth. *Math. Geol.* **1996**, *28*, 87–109. [\[CrossRef\]](#)
21. Grotzinger, J.P.; Rothman, D.H. An abiotic model for stromatolite morphogenesis. *Nature* **1996**, *383*, 423–425. [\[CrossRef\]](#)
22. Grotzinger, J.P.; Knoll, A.H. Stromatolites in Precambrian carbonates: Evolutionary mileposts or environmental dipsticks? *Annu. Rev. Earth Planet. Sci.* **1999**, *27*, 313–358. [\[CrossRef\]](#)
23. Batchelor, M.T.; Burne, R.V.; Henry, B.I.; Watt, S.D. Deterministic KPZ model for stromatolite laminae. *Physica A* **2000**, *282*, 123–136. [\[CrossRef\]](#)
24. Batchelor, M.T.; Burne, R.V.; Henry, B.I.; Watt, S.D. Mathematical and image analysis of stromatolite morphogenesis. *Math. Geol.* **2003**, *35*, 789–803. [\[CrossRef\]](#)
25. Batchelor, M.T.; Burne, R.V.; Henry, B.I.; Jackson, M.J. A case for biotic morphogenesis of coniform stromatolites. *Physica A* **2004**, *337*, 319–326. [\[CrossRef\]](#)
26. Dupraz, C.; Pattisina, R.; Verrecchia, E. Translation of energy into morphology: Simulation of stromatolite morphospace using a stochastic model. *Sediment. Geol.* **2006**, *185*, 185–203. [\[CrossRef\]](#)
27. Bosak, T.; Greene, S.; Newman, D.K. A likely role for anoxygenic photosynthetic microbes in the formation of ancient stromatolites. *Geobiology* **2007**, *5*, 119–126. [\[CrossRef\]](#)
28. Bosak, T.; Bush, J.W.M.; Flynn, M.R.; Liang, B.; Ono, S.; Petroff, A.P.; Sim, M.S. Formation and stability of oxygen-rich bubbles that shape photosynthetic mats. *Geobiology* **2010**, *8*, 45–55. [\[CrossRef\]](#)
29. Petroff, A.P.; Sim, M.S.; Maslov, A.; Krupenin, M.; Rothman, D.H.; Bosak, T. Biophysical basis for the geometry of conical stromatolites. *Proc. Natl. Acad. Sci. USA* **2010**, *107*, 9956–9961. [\[CrossRef\]](#)
30. Petroff, A.P.; Beukes, N.J.; Rothman, D.H.; Bosak, T. Biofilm growth and fossil form. *Phys. Rev. X* **2013**, *3*, 041012. [\[CrossRef\]](#)
31. Tice, M.M.; Thornton, D.C.O.; Pope, M.C.; Olszewski, T.D.; Gong, J. Archean microbial mat communities. *Annu. Rev. Earth Planet. Sci.* **2011**, *39*, 297–319. [\[CrossRef\]](#)
32. Sim, M.S.; Liang, B.; Petroff, A.P.; Evans, A.; Klepac-Ceraj, V.; Flannery, D.T.; Walter, M.R.; Bosak, T. Oxygen-dependent morphogenesis of modern clumped photosynthetic mats and implications for the Archean stromatolite record. *Geosciences* **2012**, *2*, 235–529. [\[CrossRef\]](#)
33. Reid, R.P.; James, N.P.; Macintyre, I.G.; Dupraz, C.P.; Burne, R.V. Shark Bay stromatolites: Microfabrics and reinterpretations of origins. *Facies* **2003**, *9*, 243–270.
34. Burne, R.V.; Moore, L.S. Microbialites: Organosedimentary deposits of benthic microbial communities. *Palaos* **1987**, *2*, 241–254. [\[CrossRef\]](#)
35. Kardar, M.; Parisi, G.; Zhang, Y.-C. Dynamic scaling of growing interfaces. *Phys. Rev. Lett.* **1986**, *56*, 889. [\[CrossRef\]](#)
36. Cuerno, R.; Escudero, C.; García-Ruiz, J.-M.; Herrero, M.A. Pattern formation in stromatolites: Insights from mathematical modelling. *Journal of the Royal Society: Interface* **2012**, *9*, 1051–1062. [\[CrossRef\]](#)
37. Siegesmund, M.A.; Johansen, J.R.; Karsten, U.; Friedl, T. Coleofasciculus gen. nov. (cyanobacteria): Morphological and molecular criteria for revision of the genus Microcoleus Gomont. *J. Phycol.* **2008**, *44*, 1572–1585. [\[CrossRef\]](#)
38. Gorbunov, M.Y.; Falkowski, P.G. Fluorescence induction and relaxation (FIRE) technique and instrumentation for monitoring photosynthetic processes and primary production in aquatic ecosystems. In *Photosynthesis: Fundamental Aspects to Global Perspectives*; Van der Est, A., Bruce, D., Eds.; Alliance Communications Group: Lawrence, KS, USA, 2004; pp. 1029–1031.

39. Fetisova, Z.G.; Freiberg, A.M.; Timpmann, K.E. Long-range molecular order as an efficient strategy for light harvesting in photosynthesis. *Nature* **1988**, *334*, 633–634. [\[CrossRef\]](#)
40. Buick, R.; Dunlop, J.; Groves, D. Stromatolite recognition in ancient rocks: An appraisal of irregularly laminated structures in an Early Archean chert-barite unit from North Pole, Western Australia. *Alcheringia* **1981**, *5*, 161–181. [\[CrossRef\]](#)
41. Foucher, F.; Guimbretière, G.; Bost, N.; Westall, F. Petrographical and mineralogical applications of Raman mapping. In *Raman Spectroscopy and Applications*; Maaz, K., Ed.; Pakistan Institute of Nuclear Science and Technology: Nilore, Pakistan, 2017.
42. Ketcham, R.A.; Carlson, W.D. Acquisition, optimization and interpretation of X-ray computed tomographic imagery: Applications to the geosciences. *Comput. Geosci.* **2011**, *27*, 381–400. [\[CrossRef\]](#)
43. Baker, D.R.; Mancini, L.; Polacci, M.; Higgins, M.D.; Gualda, G.A.R.; Hill, R.J.; Rivers, M.L. An introduction to the application of X-ray microtomography to the three-dimensional study of igneous rocks. *Lithos* **2012**, *148*, 262–276. [\[CrossRef\]](#)
44. Sutton, M.; Rahman, I.; Garwood, R.J. *Techniques for Virtual Palaeontology*; Wiley-Blackwell: Hoboken, NJ, USA, 2014; p. 208.
45. Noffke, N.; Christian, D.; Wacey, D.; Hazen, R.M. Microbially induced sedimentary structures recording an ancient ecosystem in the ca. 3.48 billion-year-old Dresser Formation, Pilbara, Western Australia. *Astrobiology* **2013**, *13*, 1103–1124. [\[CrossRef\]](#)
46. Gupta, P.; Diwan, B. Bacterial Exopolysaccharide mediated heavy metal removal: A Review on biosynthesis, mechanism and remediation strategies. *Biotechnol. Rep.* **2017**, *13*, 58–71. [\[CrossRef\]](#)
47. Picioreanu, C.; van Loosdrecht, M.C.M.; Heijnen, J.J. Mathematical modeling of biofilm structure with a hybrid differential-discrete cellular automaton approach. *Biotechnol. Bioeng.* **1998**, *58*, 101–116. [\[CrossRef\]](#)
48. Karatan, E.; Watnick, P. Signals, regulatory networks, and materials that build and break bacterial biofilms. *Microbiol. Mol. Biol. Rev.* **2009**, *72*, 310–347. [\[CrossRef\]](#)
49. Decho, A.W.; Frey, R.; Ferry, J. Chemical challenges to bacterial AHL signaling in the environment. *Chem. Rev.* **2011**, *111*, 86–99. [\[CrossRef\]](#)
50. Busscher, H.J.; van der Mei, H.C. How do bacteria know they are on a surface and regulate their response to an adhering state? *PLoS Pathog.* **2012**, *8*, e1002440. [\[CrossRef\]](#)
51. Decho, A.W. Microbial exopolymer secretions in ocean environments: Their role(s) in food webs and marine processes. *Oceanogr. Mar. Sci. Annu. Rev.* **1990**, *28*, 73153.
52. Williams, R.J.P. Chemical selection of elements by cells. *Coord. Chem. Rev.* **2001**, *216–217*, 583–595. [\[CrossRef\]](#)
53. Frausto da Silva, J.J.R.; Williams, R.J.P. *The Biological Chemistry of the Elements*; Oxford University Press: Oxford, UK, 2011; p. 600.
54. Geesey, G.G.; Jang, L. Interactions between metal ions and capsular polymers. In *Metal Ions and Bacteria*; Beveridge, T.J., Doyle, R.J., Eds.; John Wiley and Sons: New York, NY, USA, 1989; pp. 325–358.
55. Schultze-Lam, S.; Fortin, D.; Davis, B.S.; Beveridge, T.J. Mineralization of bacterial surfaces. *Chem. Geol.* **1993**, *132*, 171–181. [\[CrossRef\]](#)
56. Loaëc, M.; Olier, R.; Guezennec, J. Chelating properties of bacterial exopolysaccharides from deep-sea hydrothermal vents. *Carbohydr. Polym.* **1998**, *35*, 65–70. [\[CrossRef\]](#)
57. Margulis, L.; Barghoorn, E.S.; Ashendorf, D.; Banerjee, S.; Chase, D.; Francis, S.; Giovannoni, S.; Stolz, J. The microbial community in the layered sediments at Laguna Fugueroa, Baja California, Mexico: Does it have Precambrian analogues? *Precambrian Res.* **1983**, *11*, 93–123. [\[CrossRef\]](#)
58. Juniper, S.K.; Martineu, P.; Sarrazin, J.; Gélinas, Y. Microbial-mineral floc associated with nascent hydrothermal activity on CoAxial Segment, Juan de Fuca Ridge. *Geophys. Res. Lett.* **1995**, *22*, 179–182. [\[CrossRef\]](#)
59. Cameron, V.; House, C.H.; Brantley, S.L. A first analysis of metallome biosignatures of hyperthermophilic archaea. *Archaea* **2012**, *2012*. [\[CrossRef\]](#) [\[PubMed\]](#)
60. Zerkle, A.L.; House, C.H.; Brantley, S.L. Biogeochemical signatures through time as inferred from whole microbial genomes. *Am. J. Sci.* **2005**, *305*, 467–502. [\[CrossRef\]](#)
61. Robbins, L.J.; Lalonde, S.V.; Planavsky, N.J.; Partin, C.A.; Reinhard, C.T.; Kendall, B.; Scott, C.; Hardisty, D.S.; Gill, B.C.; Alessi, D.S.; et al. Trace elements at the intersection of marine biological and geochemical evolution. *Earth-Sci. Rev.* **2016**, *163*, 323–348. [\[CrossRef\]](#)
62. Moore, E.K.; Jelen, B.I.; Giovannelli, D.; Raanan, H.; Falkowski, P.G. Metal availability and the expanding network of microbial metabolisms in the Archean eon. *Nat. Geosci.* **2017**, *10*, 629–636. [\[CrossRef\]](#)

63. Armendariz, A.L.; Talano, M.A.; Wevar Oller, A.L.; Medina, M.I.; Agostini, E. Effect of arsenic on tolerance mechanisms of two plant growth-promoting bacteria used as biological inoculants. *J. Environ. Sci.* **2015**, *33*, 203–210. [[CrossRef](#)] [[PubMed](#)]
64. Nocelli, N.; Bogino, P.C.; Banchio, E.; Giordano, W. Roles of Extracellular polysaccharides and biofilm formation in heavy metal resistance of Rhizobia. *Materials* **2016**, *9*, 418. [[CrossRef](#)] [[PubMed](#)]
65. Sánchez-Román, M.; Fernáández-Remolar, D.; Amils, R.; Saánchez-Nava, A.; Schmid, T.; Martin-Uriz, P.S.; Rodríguez, N.; McKenzie, J.A.; Vasconcelos, C. Microbial mediated formation of Fe-carbonate minerals under extreme acidic conditions. *Sci. Rep.* **2014**, *4*, 4767. [[CrossRef](#)] [[PubMed](#)]
66. Orange, F.; Disnar, J.-R.; Gautret, P.; Westall, F.; Bienvenu, N.; Lottier, N.; Prieur, D. Preservation and Evolution of organic matter during experimental fossilisation of the hyperthermophilic Archaea *Methanocaldococcus jannaschii*. *Orig. Life Evolut. Biosph.* **2012**, *42*, 587–609. [[CrossRef](#)]
67. Walter, M.R.; Buick, R.; Dunlop, J.S.R. Stromatolites 3400–3500 Myr old from the North Pole area, Western Australia. *Nature* **1980**, *284*, 443–445. [[CrossRef](#)]
68. Ueno, Y.; Maruyama, S.; Isozaki, Y.; Yurimoto, H. Early Archean (ca. 3.5 Ga) microfossils and ¹³C-depleted carbonaceous matter in the North Pole area, Western Australia: Field occurrence and geochemistry. In *Geochemistry and the Origin of Life*; Nakashima, S., Maruyama, S., Brack, A., Windley, B.F., Eds.; Universal Academy Press Inc.: Tokyo, Japan, 2001; pp. 201–236.
69. Lanier, W.P. Approximate growth rates of Early Proterozoic Microstromatolites as deduced by biomass productivity. *Palaios* **1986**, *1*, 525–542. [[CrossRef](#)]
70. Kazmierczak, J.; Kempe, S. Genuine modern analogues of Precambrian stromatolites from caldera lakes of Niufo’ou Island, Tonga. *Naturwissenschaften* **2006**, *93*, 119–126. [[CrossRef](#)] [[PubMed](#)]
71. Allwood, A.C.; Walter, M.R.; Burch, I.W.; Kamber, B.S. 3.43 billion-year-old stromatolite reef from the Pilbara Craton of western Australia: Ecosystem-scale insights to early life on Earth. *Precambrian Res.* **2007**, *158*, 198–227. [[CrossRef](#)]
72. Harwood, C.L.; Sumner, D.Y. Origins of microbial microstructures in the Neoproterozoic Back Spring Dolomite: Variations in microbial community and timing of lithification. *J. Sediment. Res.* **2012**, *82*, 709–722. [[CrossRef](#)]
73. de Wit, M.; Hart, R.; Martin, A.; Abbott, P. Archean abiogenic and probable biogenic structures associated with mineralized hydrothermal vent systems and regional metasomatism, with implications for greenstone belt studies. *Econ. Geol.* **1982**, *77*, 1783–1802. [[CrossRef](#)]
74. Lindsay, J.F.; Brasier, M.D.; McLoughlin, N.; Green, O.R.; Fogel, M.; Steele, A.; Mertzman, S.A. The problem of deep carbon—An Archean paradox. *Precambrian Res.* **2005**, *143*, 1–22. [[CrossRef](#)]
75. McLoughlin, N.; Wilson, L.A.; Brasier, M.D. Growth of synthetic stromatolites and wrinkle structures in the absence of microbes – Implications for the early fossil record. *Geobiology* **2008**, *6*, 95–105. [[CrossRef](#)] [[PubMed](#)]
76. Shepard, R.N.; Sumner, D.Y. Undirected motility of filamentous cyanobacteria produces reticulate mats. *Geobiology* **2010**, *8*, 179–190. [[CrossRef](#)]
77. Flannery, D.T.; Walter, M.R. Archean tufted microbial mats and the Great Oxidation Event: New insights into an ancient problem. *Aust. J. Earth Sci.* **2011**, *59*, 1–11. [[CrossRef](#)]
78. Williams, R.J.P.; Frausto da Silva, J.J.R. Evolution was chemically constrained. *J. Theor. Biol.* **2003**, *220*, 323–343. [[CrossRef](#)]
79. Hofmann, A. Archean hydrothermal systems in the Barberton greenstone belt and their significance as a habitat for early life. In *Earliest Life on Earth: Habitats, Environments and Methods of Detection*; Golding, S.D., Glikson, M., Eds.; Springer Science and Business Media: Berlin, Germany, 2011; pp. 51–78.
80. Buick, R. When did oxygenic photosynthesis evolve? *Philos. Trans. R. Soc. Lond. B* **2008**, *363*, 2731–2743. [[CrossRef](#)]
81. Sforna, M.C.; Philippot, P.; Somogyi, A.; van Zuilen, M.A.; Medjoubi, K.; Schoepp-Cothenet, B.; Nitschke, W.; Visscher, P.T. Evidence for arsenic metabolism and cycling by organisms 2.7 billion years ago. *Nat. Geosci.* **2014**, *7*, 811–815. [[CrossRef](#)]

